Journal Pre-proof

Distortion of passive scalar structure during suction-based plume sampling

Aaron C. True, John P. Crimaldi

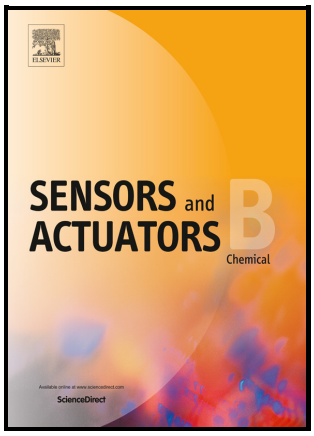

PII: S0925-4005(22)00660-8

DOI: https://doi.org/10.1016/j.snb.2022.132018

Reference: SNB132018

To appear in: *Sensors and Actuators: B. Chemical*

Received date: 6 January 2022
Revised date: 13 April 2022
Accepted date: 6 May 2022

Please cite this article as: Aaron C. True and John P. Crimaldi, Distortion of passive scalar structure during suction-based plume sampling, *Sensors and Actuators: B. Chemical,* (2022) doi:https://doi.org/10.1016/j.snb.2022.132018

Graphical Abstract

Distortion of passive scalar structure during suction-based plume sampling

Aaron C. True, John P. Crimaldi

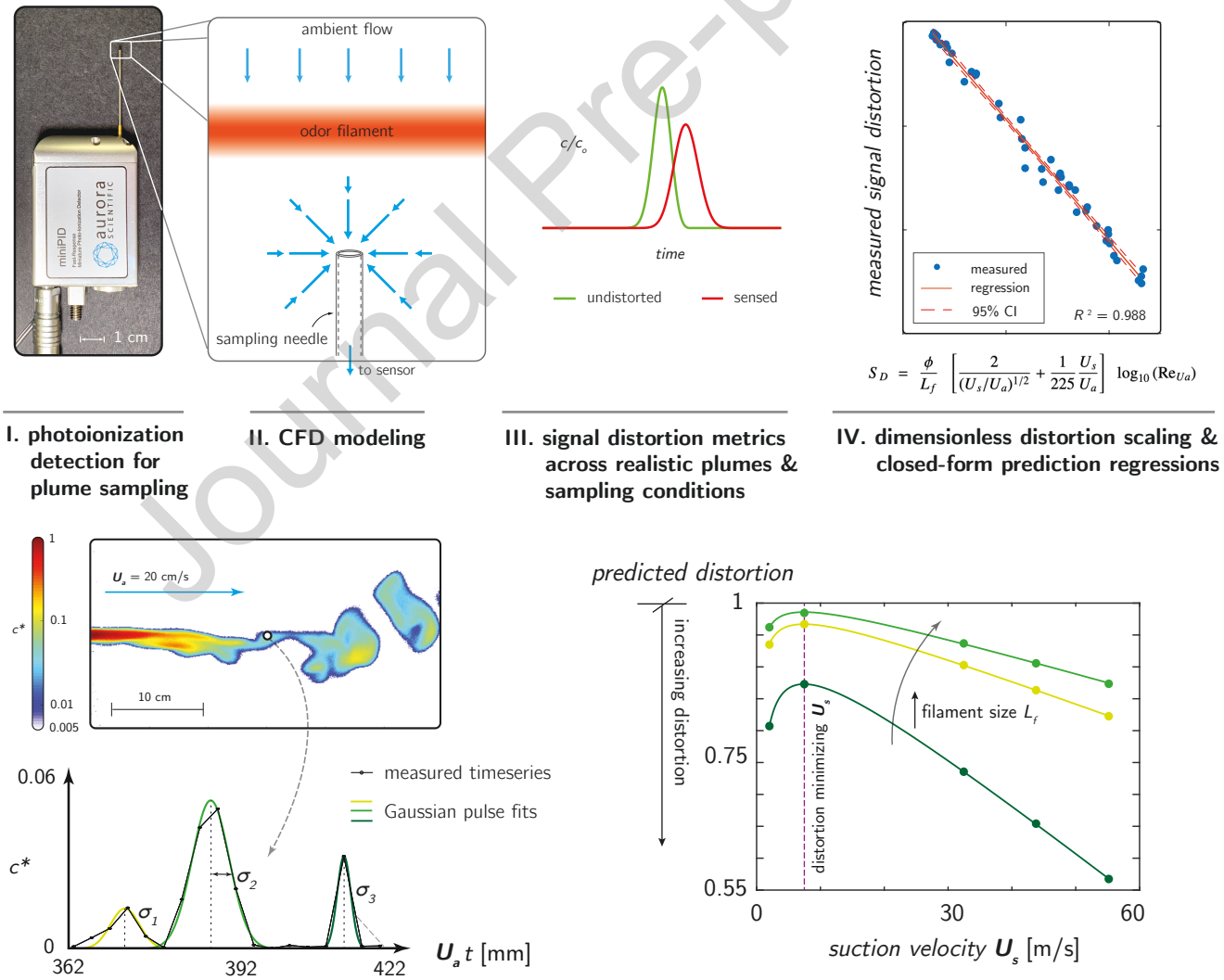

Highlights

Distortion of passive scalar structure during suction-based plume sampling

Aaron C. True, John P. Crimaldi

- Modeled photoionization detector (PID) gas sampling using computational fluid dynamics
- Parameterized PID distortion levels for a range of realistic plume conditions
- Created regressions that predict distortion levels given PID operational parameters
- Identified distortion mitigation strategies for a common commercially-available PID through suction velocity tuning
- Produced insights for other suction-based plume sensing schemes through dimensionless distortion scaling parameter and prediction regressions

Distortion of passive scalar structure during suction-based plume sampling

Aaron C. True[1,1], John P. Crimaldi[1]

[a]*Department of Civil, Environmental, & Architectural Engineering, University of Colorado, 428 UCB, Boulder, Colorado, 80309, USA*

Abstract

Studies of plume dynamics and olfaction often rely on photoionization detectors (PID) to quantify spatiotemporal distributions of passive scalars (gases, vapors, odors). However, the potential for PID suction to distort filaments and to modify the resulting sensed time record remains unclear. We used computational fluid dynamics to model a widely-used PID to quantify and parameterize suction distortion by considering how sensed concentration records compare to those registered by an ideal probe absent distorting effects. Models cover a range of realistic plume conditions, and we show that PID can modify the peak concentration and pulse shape of sensed records, with peak amplitude reduced by up to 45% and pulse width increased by up to 100% for the cases considered here. We quantified how distortion varies in three key nondimensional parameters describing PID geometry and plume sampling conditions: relative suction rate, relative filament size, and ambient flow Reynolds number. We combined analytical and numerical tools with dimensional analysis and scaling arguments to interpret results and discuss when distortion is likely and what drives it. We built a dimensionless distortion scaling parameter and simple regressions capable of predicting distortion levels, and our results enable PID users to estimate distortion levels and to employ mitigation strategies through suction velocity tuning. We show that an ideal relative suction rate (ratio of suction-to-ambient velocities) near 30 minimizes distortion universally for the Aurora Scientific miniPID. The findings and discussion herein can inform distortion-mitigating design principles and best sampling practices for other suction-based passive scalar sensing schemes.

Keywords: photoionization detector, plume dynamics, suction flow, passive scalars, distortion, odors
PACS: 0000, 1111
2000 MSC: 0000, 1111

1. Introduction

Photoionization detectors (PID) are widely used in studies and applications related to olfaction [1, 2] and plume dynamics [3, 4, 5], providing quantitative gas concentration measurements in fields ranging from neuroscience [6, 7, 8, 9, 10, 11, 12] and ecology [13] to atmospheric science [14, 15], robotics [16], public health [17], and defense [18]. PIDs produce and register a voltage response created when an ionizable gas constituent is subjected to UV radiation in an ionization chamber [19]; this response is proportional to gas concentration. While PID designs and technologies continue to evolve for improved functionality and customized applications [20, 21, 22], the traditional suction-based PID (Fig. 1) that actively draws samples through a round needle and into the ionization chamber has been widely used across disciplines for decades [23, 24]. The fluid dynamics governing suction-based sampling schemes are relevant to numerous engineering applications and biological systems [25, 26, 27, 28]. The role that suction plays in modifying the flow field around the sampler, and by extension the transport and diffusion of entrained entities of interest (e.g., inertial particles or diffusive passive scalars) is critical to understand and quantify.

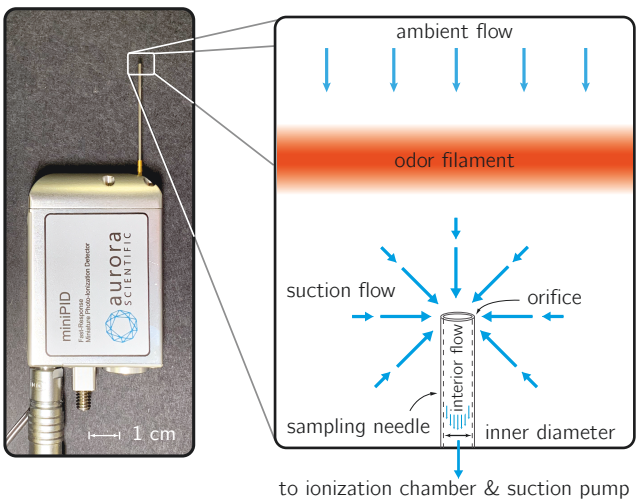

Figure 1: A common PID (Aurora Scientific 200B miniPID) that uses suction to draw airborne scalar filaments through an orifice, into a sampling needle, and downstream to the ionization chamber and sensor location. The combined ambient, suction, and interior needle flows may distort the spatiotemporal structure of a sampled filament and affect temporal characteristics of the concentration record at the sensor level.

Email addresses: aaron.true@colorado.edu (Aaron C. True), crimaldi@colorado.edu (John P. Crimaldi)

For clarity and historical context, we distinguish *samplers* from *probes*; samplers are active sensors that use suction to draw fluid-borne samples through an orifice and into a tube-like conveyance leading to a sensor while probes are generic bluff body sensors placed into some flow of interest. Extensive bodies of literature detail various aspects of sampler- and probe-induced measurement artifacts (see below), broadly referred to here as *distortion*. Distortion here describes any departure of signal characteristics measured at the sensor level from those produced by an ideal (non-intrusive) probe that does not modify the local flow field or by extension the spatiotemporal structure of an entrained entity of interest (e.g., passive scalar filaments). In the case of suction-based samplers, distorting effects arising in both the *exterior* and *interior* flows (the unconstrained flow outside of the sampling tube and the pipe flow inside the tube leading to the sensor, respectively, Fig. 1, right panel) may be relevant, depending on operational conditions. Considering the spatiotemporal structure of the PID sampling flow field, from the exterior farfield away from the orifice to the sensor far down the needle, distorting effects may originate from a range of mechanisms in both the interior and exterior flow regions. These are covered in detail in the discussion section below.

In the aerosol sciences, an extensive and historic body of literature describes how suction-based samplers affect aspiration and transmission efficiencies (ratios of aspirated-to-ambient aerosol concentration and sampled-to-aspirated particles, respectively) [29]. These effects are generally considered in different regions of the flow. In the exterior flow approaching the sampling orifice, inertial particle effects, including bypass and impaction on the tube, potentially alter the aspiration efficiency [30, 31, 32, 33]. In the interior pipe flow of the sampling tube, transmission efficiencies may also suffer due to artifacts associated most notably with inertial and turbulent inertial deposition, sedimentation, and diffusion [34, 15, 35]. An ideal aerosol sampler is thus one that draws isoaxially (main axis of the tube aligned with the mean ambient flow vector) and isokinetically (cross-sectional average tube velocity equal to the ambient flow speed), minimizing measurement artifacts relative to the true (undistorted) signal of interest. Despite the common fluid dynamics governing suction-based sampling of aerosols and passive scalars, the complexities of inertial particle dynamics [36] obscure robust insights into how suction-based sampling schemes might alter the spatiotemporal structure of diffusive passive scalars, and potentially modify the resulting concentration records at the sensor level.

In the atmospheric sciences, the interactions of passive scalar structures with ground- and aircraft-mounted probes is of considerable interest in the context of producing accurate eddy covariance measurements, which requires simultaneous sensing of turbulent velocity and scalar concentration fluctuations [37]. Most historic studies employed probe-based scalar concentration measurement systems, and corresponding investigations characterized how the distortion from a generic bluff body in a flow (i.e. a probe) affects the spectral characteristics of recorded concentration fluctuations in regimes relevant to tower- or aircraft-mounted probes [38, 39]. More recent eddy covariance measurement systems have employed suction-based samplers for scalar measurements [40]; however, the exploration of sampler-induced measurement artifacts was limited to finding the optimal spacing between scalar sampler (e.g., PID) and the flow sensor (hot-wire anemometer) such that the turbulent velocity measurements were unimpacted by the suction flow.

Despite valuable insights from the literature into the structure of the exterior suction-induced flow field [41, 31] and how the interior pipe flow attenuates scalar concentration fluctuations [42], including the effects of intake sections and pipe bends [43], there remains a clear need for a study providing parametric characterization of scalar distortion during measurement by suction-based samplers, including PID. In particular, there is considerable value in understanding how suction flows might modify the spatiotemporal structure of scalar filaments of interest, and how that modification might impact the temporal signal characteristics at the sensor level. In this paper, we present a computational fluid dynamics model of a commonly-used, commercially-available PID (Aurora Scientific 200B miniPID). Based on a dimensional analysis of idealized suction-based scalar sampling, we explore a nondimensional parameter space spanning a range of realistic plume and sampling conditions. We quantify PID-induced measurement artifacts through two main distortion metrics, and build regressions capable of predicting distortion levels as a function of operational conditions. Finally, we discuss the fluid physics relevant to different distortion mechanisms that might arise during suction-based sampling schemes and provide guidance on distortion mitigation strategies.

2. Methodology

2.1. Overview and definitions

We modeled idealized filament-suction interaction during PID sampling by considering a diffusive, Gaussian passive scalar filament of prescribed width L_f being advected at speed U_a in a steady, uniform ambient flow towards a PID needle sampling with volumetric suction flowrate Q (Fig. 2a). L_f is defined as the 2σ streamwise filament width at the instant when the leading edge arrives at the edge of the suction distortion zone (introduced and described below), where σ is the spatial standard deviation of the Gaussian filament (*pulse half-width*). The model is parameter-matched in geometry (needle diameter ϕ, needle length L_n, needle wall thickness δ) and flow parameters (range of Q) to the Aurora Scientific 200B miniPID (Table 1). Numerical simulations were performed via finite element discretization of the Navier-Stokes and continuity equations governing the exterior and interior sampling flow fields (Fig. 2b,c), in addition to the nonreactive advection-diffusion equation governing the transport and diffusion of passive scalar filaments (Fig. 2b,d). The three-dimensional axisymmetric model domain includes the flow exterior to the needle, extending far from the suction distortion field near the orifice, as well as the interior pipe flow of the needle, up to the sensor location in the ionization chamber. Model runs were selected to

cover a broad nondimensional parameter space containing a range of realistic plume conditions (U_a and L_f) and PID suction flowrates Q (Table A.6). These include the three standard Q of the 200B miniPID (Table 1), in addition to one hypothetical ultra-low Q of 0.225 L/min. This is physically achievable with a potentiometer-type adjustment on the suction pump, and adjusting the suction flowrate Q (equivalently the characteristic suction velocity U_s defined below) allows a PID user to modify the relative suction rate U_s/U_a (defined below) of the sampler. This may often be the only viable adjustment mechanism available for distortion mitigation.

Table 1: Summary of PID geometry and flow parameters for the Aurora Scientific 200B miniPID, as well as fluid and odorant properties used in the numerical models. Properties are listed at 15^{o}C, and the molecular diffusivity value listed is for propylene in air.

PID parameters	
inner diameter ϕ [mm]	0.76
needle length L_n [mm]	57
needle wall thickness δ [mm]	0.255
L_n/ϕ	75
δ / ϕ	0.34
δ / L_n	0.0045
suction rates Q [L/min]	0.9, 1.2, 1.5
suction velocities U_s [m/s]	33, 44, 55
fluid and odorant properties	
kinematic viscosity ν [m^2/s]	1.48E-05
dynamic viscosity μ [kg/(mm·s)]	1.81E-08
density ρ [kg/m^3]	1.225
molecular diffusivity D [mm^2/s]	12.4
Schmidt number Sc	1

An important tool used herein to analyze and interpret PID sampling distortion data is built on the application of an analytical potential flow description of the suction flow field. The three-dimensional point sink flow (Fig. 3a) describes inviscid, steady flow radially converging towards the sink (analogous to the needle orifice), where the magnitude of the suction velocity decays with radial distance from the orifice ($1/r^2$) for a given volumetric sink strength Q (analogous to the PID suction flowrate). The local sink velocity is then

$$\mathbf{u_s}(\mathbf{r}) = -\frac{Q}{4\pi\mathbf{r}^2} \ . \tag{1}$$

The unidirectional and inviscid sink flow description is ultimately limited in its ability to capture the true structure of the exterior sampling flow, particularly in the direct vicinity of the orifice where the flow structure is dominated by the impermeability and no-slip conditions along the PID needle walls and by the directional flow boundary condition at the orifice [25]. However, as shown and discussed below, the sink flow description does accurately capture key features of the overall spatial structure of the PID suction flow, specifically along the axis of the needle and at distances greater than approximately one needle diameter from the orifice.

Applying the sink flow solution described above, we derived an important lengthscale describing the spatial extent of the PID suction distortion zone L_s (Fig. 3b). For a PID sampling with suction flowrate Q through a needle of diameter ϕ, the resulting cross-sectional average velocity in the needle is the characteristic suction velocity

$$U_s = \frac{4Q}{\pi\phi^2} \ . \tag{2}$$

For a PID sampling isoaxially in a uniform flow of speed U_a, the size of the suction distortion zone L_s is defined as the distance from the needle orifice at which the local suction velocity induced by the PID has decayed to the ambient flow velocity U_a. Using the analytical sink flow description of the local sink velocity (Eq. 1), the suction distortion lengthscale is given by

$$L_s = \frac{\phi}{2}\left(\frac{U_s}{U_a}\right)^2 \ , \tag{3}$$

where U_s/U_a is the relative suction rate of the PID. The length L_s is the diameter of a spherical region centered on the orifice in which the local suction-induced velocity is stronger than the ambient flow velocity, i.e. the *suction distortion zone*. Note that the formulation in Eq. 3 is the full-width of the suction distortion zone, and it is often convenient to consider the corresponding half-width, differing only by a factor of two.

An advective timescale associated with the suction distortion zone can be derived based on the ambient velocity

$$T_{L_s} = \frac{L_s}{U_a} \ , \tag{4}$$

representing the residence time of a point or feature in the suction distortion field (e.g., the interface between scalar filament and ambient fluid). Another important advective timescale is the time required for the scalar filament width to pass through a point in space

$$T_{L_f} = \frac{L_f}{U_a} \ . \tag{5}$$

The total residence time of a filament of size L_f traveling through the suction distortion zone of full-width L_s at speed U_a is then

$$T_R = \frac{L_s + L_f}{U_a} \ . \tag{6}$$

The needle residence time (orifice-to-sensor) is similarly

$$T_{L_n} = \frac{L_n}{U_s} \ . \tag{7}$$

These and related timescales are useful for analyzing and interpreting distortion data below.

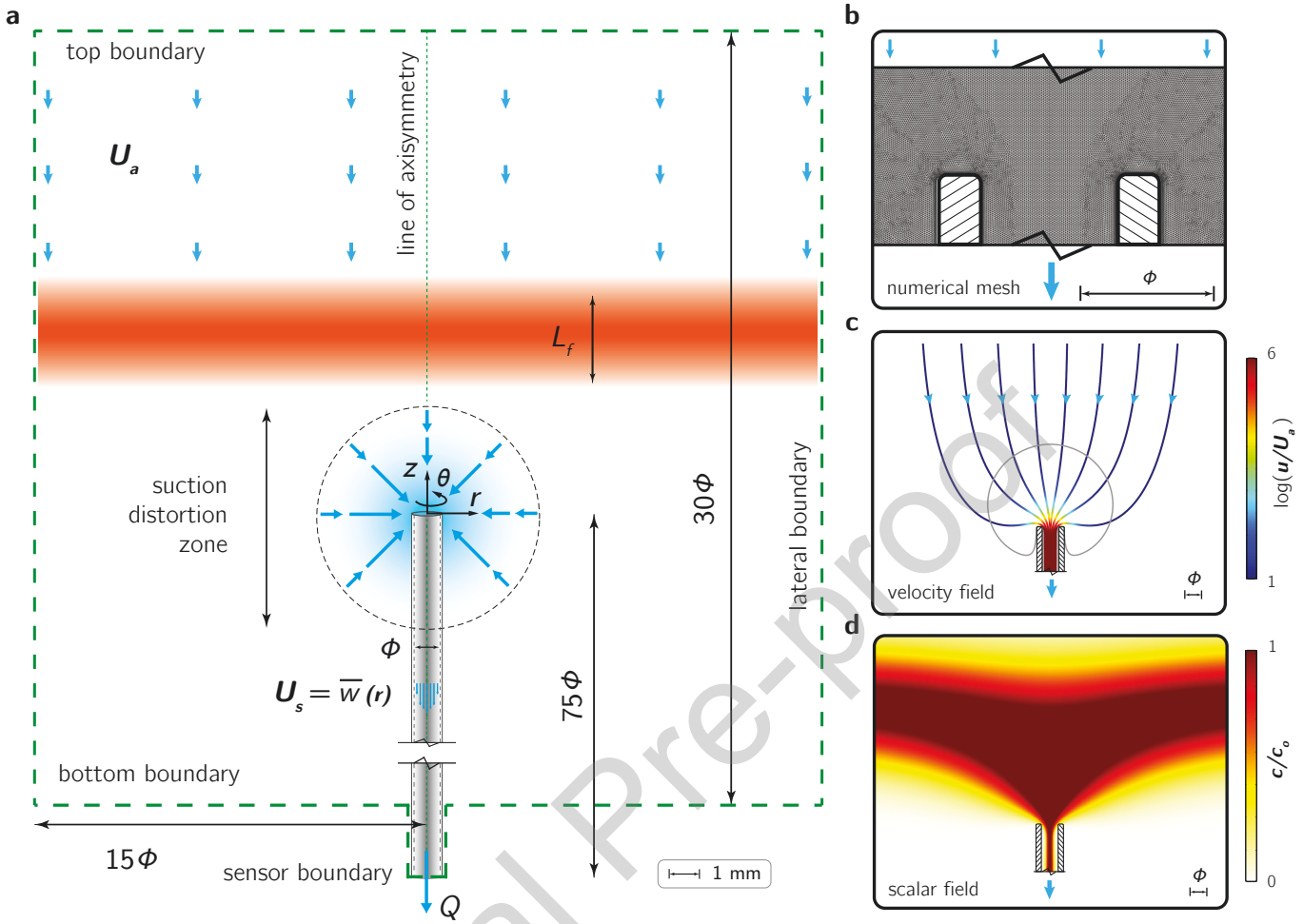

Figure 2: **a.** The three-dimensional axisymmetric model domain in which a scalar filament of prescribed width L_f is advected in an ambient flow (U_a) towards a PID needle sampling with volumetric suction rate Q. The spatial extent of the model domain was iteratively selected to eliminate boundary effects on the resulting flow field and scalar transport and diffusion dynamics. **b.** A detailed view of the finite element (FEM) mesh near the PID needle orifice, the region of the model domain that contains the strongest fluid velocity and scalar concentration gradients. The needle walls are denoted as black rectangles with cross-hatching. Note the highly-resolved mesh and the local refinement along the needle walls suitable for accurately resolving boundary layers and other strong gradients here. **c.** A representative flow field showing fluid streamlines colored by normalized velocity magnitude (log-scale) and the extent of the suction distortion zone (L_s), indicated by the gray contour line where the normalized local velocity u/U_a equals two. **d.** A representative scalar concentration field showing filament-suction interaction through source-normalized odor concentrations contours.

2.2. *Governing equations and parameterization*

The axisymmetric nondimensional flow field $\mathbf{u}^* = [u^*, w^*]$ with radial (r^*) and axial (z^*) velocity components u^* and w^* is governed by the nondimensional, incompressible, Navier-Stokes and continuity equations

$$\frac{\partial \mathbf{u}^*}{\partial t^*} + \mathbf{u}^* \cdot \nabla^* \mathbf{u}^* = -\nabla^* p^* + \mathrm{Re}^{-1} \nabla^{*2} \mathbf{u}^* + \mathbf{g}^* \tag{8}$$

and

$$\nabla^* \cdot \mathbf{u}^* = 0\,, \tag{9}$$

where length, time, velocity, and pressure have been nondimensionalized by ϕ, ϕ/U_s, U_s, and ρU_s^2, respectively, and where $\mathbf{g}^* = \phi \mathbf{g}/U_s^2$. Here and elsewhere we denote vector quantities in bold face, scalar quantities in plain face, and non-dimensional quantities with an asterisk. Note that the flow field governed by Eqns. 8 and 9 is controlled by the single nondimensional parameter Re, the Reynolds number describing the relative importance of inertial and viscous flow effects as

$$\mathrm{Re} = \frac{UL}{\nu}\,, \tag{10}$$

based on a characteristic velocity (U), lengthscale (L), and the fluid kinematic viscosity ν. The nondimensional passive scalar concentration field c^* is governed by the coupled nondimensional, nonreacting advection-diffusion equation

$$\frac{\partial c^*}{\partial t^*} + \mathbf{u}^* \cdot \nabla^* c^* = \mathrm{Pe}^{-1} \nabla^{*2} c^*; \tag{11}$$

where scalar concentration c has been nondimensionalized by the source (maximum) concentration c_o, and velocity and time are nondimensionalized as in Eqns. 8 and 9. Note that the scalar concentration field governed by Eq. 11 is controlled by a single

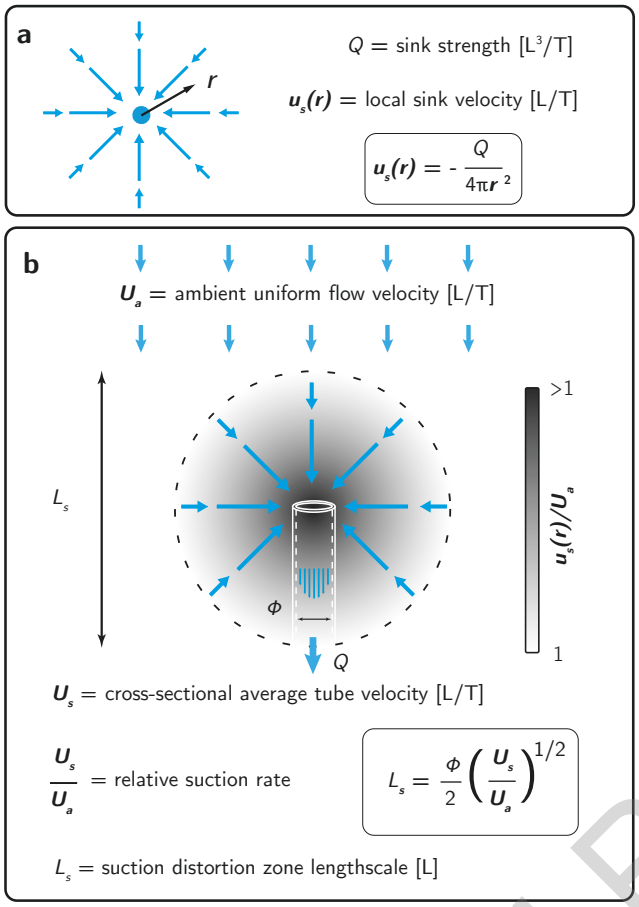

Figure 3: **a.** The potential flow field resulting from a steady, inviscid, three-dimensional point sink provides a useful first-order approximation for the suction flow generated by a sampling PID. **b.** The suction distortion lengthscale L_s is derived from the potential flow solution, and is defined as the point in space where the local suction velocity $u_s(r)$ has decayed to the ambient flow speed U_a. L_s is a function of needle geometry and relative suction rate U_s/U_a.

nondimensional parameter representing the relative importance of advective versus difussive scalar transport mechanisms, the Péclet number Pe,

$$\mathrm{Pe} = \frac{UL}{D} = \mathrm{ReSc}\ , \tag{12}$$

where the Schmidt number Sc is the ratio of the momentum diffusivity of the ambient fluid ν (i.e. kinematic viscosity) to the mass diffusivity of the given passive scalar in the ambient fluid D. Different formulations of Re and Pe (Eqns. 10 and 12) based on different characteristic velocities (suction U_s versus ambient U_a) and length scales (ϕ, L_s, etc.) are often useful and are used herein and denoted appropriately. Note that the nondimensional relative suction rate U_s/U_a identified in the dimensional analysis described next can used to algebraically relate different formulations of Re and Pe.

Dimensional analysis of idealized filament-suction interaction during PID sampling, considered here and depicted in Fig. 2a, defines a parameter space of nondimensional variable groupings upon which nondimensional signal distortion should depend. These include PID geometric ratios (fixed here to match the Aurora Scientific 200B miniPID), as well as ratios parameterizing the flow and scalar transport and diffusion dynamics (Table 2).

Table 2: Summary of important nondimensional parameters resulting from a dimensional analysis of nondimensional distortion levels during the idealized filament-suction interaction problem describing PID sampling.

parameter	significance
L_n/ϕ	relative needle length
$\delta\ /\ \phi$	relative wall thickness
L_f/ϕ	relative filament size
U_s/U_a	relative suction rate
$U\phi/\nu$	Reynolds number, Re
$U\phi/D$	Péclet number, Pe

The filament-suction interaction problem is thus fully parameterized by the relative geometry of the PID, the relative filament size of the scalar filament L_f/ϕ, the relative suction rate U_s/U_a, and a single formulation of the Reynolds number (Eqn. 10) and Peclet number (or alternatively the Schmidt number Sc, Eqn. 12). This is true for a PID sampling isoaxially (scalar concentration gradient and suction velocity are both parallel to the ambient flow vector) in a steady and uniform ambient flow environment (non-turbulent), far from any solid surfaces excepting the PID needle itself. In our models, PID geometry and ambient fluid and odorant properties are fixed (Table 1) such that we expect measured (modeled) variations in nondimensional distortion levels to depend on relative filament size L_f/ϕ, relative suction rate U_s/U_a, and ambient Reynolds number Re_{Ua}.

The two distortion metrics used herein to compare characteristics of the temporal concentration records sensed by the PID (*sensed*) versus registered by an ideal (non-intrusive) probe in the absence of distorting effects (*undistorted*) are the nondimensional peak amplitude ratio c_p^*

$$c_p^* = \frac{c_p^{'}}{c_p} \tag{13}$$

and pulse width ratio σ^*

$$\sigma^* = \frac{\sigma^{'}}{\sigma}\ , \tag{14}$$

where the prime denotes the sensed value. The sensor level signal is integrated across the needle diameter at the sensor boundary in the model, consistent with how the 200B miniPID operates, and the undistorted signal comes from an ideal probe located at the same location as the needle orifice but in the absence of any distorting effects (i.e. related to the needle itself or the suction distortion field). These two metrics characterize distortion-related pulse attenuation and are shown conceptually in Fig. 4. Other distortion effects such as modification of peak arrival time or higher-order pulse shape effects (skewness and kurtosis) are less informing about suction-induced distortion overall since the former simply relates to changes in advection timescales here (and can be accounted for), and for the later,

the lower-order metrics used here are loosely coupled to higher-order effects. Note that while c_p^* and σ^* are closely related (as shown below), they are not explicitly coupled, for example by a scalar mass conservation constraint for the sensed versus undistorted pulses (proportional to the area under the curves).

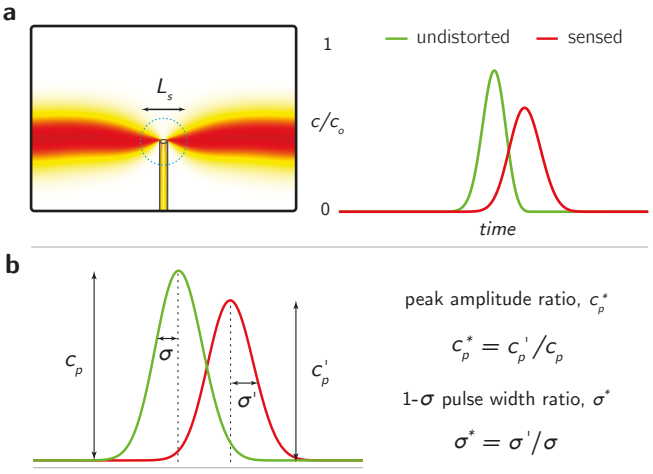

Figure 4: **a.** Nondimensional distortion metrics quantifying differences in the temporal scalar concentration pulse shapes between the sensor (*sensed*, red line) and that expected from an ideal probe, in the absence of the PID and its suction distortion field (*undistorted*, green line). **b.** The peak amplitude ratio c_p^* is defined as the ratio of sensed-to-undistorted peak concentration such that $0 < c_p^* \leq 1$. The pulse width ratio σ^* is defined as the ratio of the temporal pulse width 2σ of the sensed-to-undistorted concentration pulse such that $1 \leq \sigma^*$.

2.3. Numerical methods and modeling

Numerical simulations were performed via finite element discretization of the Navier-Stokes and continuity equations (Eqs. 8 and 9) governing fluid flow, and the coupled, nonreactive advection-diffusion equation (Eqn. 11) governing scalar transport and diffusion. The COMSOL Multiphysics package (ver. 5.6) was used to generate the mesh in the axisymmetric model domain depicted in Fig. 2a and to solve the system of equations resulting from the weak (integral) form discretization of the governing equations, subjected to prescribed initial and boundary conditions.

2.3.1. Model domain and meshing

The unstructured finite-element mesh contained triangular and quadrilateral elements locally refined in spatial regions with strong fluid velocity or scalar concentration gradients, including around the orifice and along needle walls. Mesh refinement was also warranted in a region along the top inlet boundary of the model where scalar filaments were introduced as a Gaussian concentration boundary condition in time (details below), to mitigate potential numerical instabilities associated with small L_f and/or high U_a. A mesh refinement study was performed to test for solution convergence throughout the domain. We iterated to finer meshes (increasing model degrees of freedom) until the total relative error estimate summed over all elements and degrees of freedom was of order 1E-6, and there was no discernible change in the solutions describing the fluid velocity and scalar concentration fields with further grid refinement. The final mesh implemented for all model runs had typical maximum and minimum element sizes (spatial resolution) of approximately 10 and 4 μm, respectively, with approximately 85 mesh elements across the needle orifice (diameter $\phi = 0.76$ mm). The corners on the end of the needle at the orifice location were filleted with a small radius of 50 μm to eliminate potential numerical instabilities originating at an otherwise sharp-edged discontinuity, shown to scale in Fig. 2b. In addition to the mesh refinement study, we assessed model convergence and performance using several metrics and considerations for both the fluid velocity and scalar concentration fields throughout the parameter space modeled (see below, Table A.6).

2.3.2. Initial and boundary conditions

Initial conditions were $\mathbf{u}^* = 0$, $p^* = 0$ and $c^* = 0$ everywhere. The needle walls were impermeable, no-slip conditions, $\mathbf{u}^* = 0$, with zero total scalar flux normal to the wall everywhere, $-\mathbf{n} \cdot (\mathbf{J} + \mathbf{u}^* c^*) = 0$. The diffusive component of the total flux $\mathbf{J} = -\mathbf{n} \cdot D\nabla c$, and $\mathbf{u}^* c^*$ is the advective flux; $\mathbf{n}$ is the unit vector normal to the needle wall everywhere.

For the range of suction Reynolds numbers modeled (Table A.6), the interior flow of the needle remains laminar and the transient timescale for the viscous development of the exterior flow ($T_{trans} = (\phi^2/\nu)/\mathrm{Re}$) is extremely short [25], such that the flow field quickly reaches a quasi-steady state. For computational efficiency, we therefore implemented a steady (stationary) solver for the fluid flow field (details below), produced by the combined ambient and suction flow fields which are initiated to their prescribed values at time $t^* \geq 0$. The ambient flow was prescribed as an inlet condition along the top boundary of the model, specifying normal, uniform flow with speed U_a, $\mathbf{u} = -U_a\mathbf{n}$. The PID suction flow was prescribed as an outlet boundary condition at the sensor location (bottom end of the needle) of fully-developed (laminar) normal flow with constant cross-sectional average needle velocity equal to the characteristic suction velocity U_s (equivalent to specifying the suction flowrate Q, Eqn. 9). A coupled ODE computes p_{exit}^* such that the desired average outlet velocity is achieved under laminar flow conditions: $L_{exit}\nabla_t^* \cdot [-p^*\mathbf{I} + \mu(\nabla_t^*\mathbf{u}^* + (\nabla_t^*\mathbf{u}^*)^T)] = -p_{exit}^*\mathbf{n}$ where $\mathbf{I}$ is the identity matrix, ∇_t^* is the tangential gradient, and $\mathbf{n}$ is the unit vector normal to the outlet boundary. L_{exit} is the length of a virtual channel extending downstream of the outlet (sensor), and p_{exit} is the pressure constant applied at the end of this virtual channel to sustain laminar flow of specified cross-sectional average velocity U_s across the sensor boundary. This outlet boundary condition is effectively a normal stress condition, together with a no tangential stress condition, a typical formulation for an outlet boundary condition [44]. This formulation results in a numerically well-posed problem and avoids convergence problems when specifying the desired velocity condition at the top boundary inlet. The lateral and bottom domain boundaries were no normal stress, open boundaries through which fluid could enter and leave the domain, prescribed as $[-p^*\mathbf{I} + \mu(\nabla^*\mathbf{u}^* + (\nabla^*\mathbf{u}^*)^T)]\mathbf{n} = 0$. Specifying zero normal force enforces that the pressure is balanced by the

viscous shear force on the boundaries which is true when the normal gradient of the normal velocity is small there.

Scalar filaments were introduced into the sampling flow field by prescribing a temporal Gaussian concentration pulse at the top inlet boundary of the model domain (Figs. 2a and 4). The standard deviation of the Gaussian concentration pulse specified at the inlet was such that the temporal pulse width σ_T mapped to the desired spatial pulse width σ_L at the top boundary of the model as

$$\sigma_L = U_a \sigma_T \tag{15}$$

for a given ambient flow speed U_a. The specific value of σ_L dictated was such that, following diffusive broadening during the advection time from the inlet boundary, the spatial 2σ filament pulse width at the instant when the leading edge arrives at the upstream edge of the suction distortion zone ($z = L_s$, half-width) is the controlled value L_f. The relationship between the pulse widths at the inlet σ_{inlet} and upon arrival at the suction distortion zone is

$$\sigma_{L_s}^2 \approx \sigma_{inlet}^2 + 2D\Delta t \ . \tag{16}$$

following advection time Δt. The scalar boundary condition at the lateral, bottom, and sensor boundaries was no diffusive flux normal to the boundary $-\mathbf{n} \cdot \mathbf{J} = -\mathbf{n} \cdot D\nabla c = 0$.

2.3.3. Discretization schemes and solvers

Lagrangian shape functions were used for weak-form discretization of the fluid velocity, pressure, and scalar concentration fields. The order of the numerical integration scheme was matched to the order of the element for each dependent variable (all first-order here). The time-dependent (unsteady) solver used for the scalar concentration field employs an implicit backward differentiation formula (BDF) method with maximum second order schemes, balancing numerical stability and damping tendencies for our gradually varying flows with smooth velocity and scalar concentration gradients. BDF methods use variable-order, variable step-size backward differentiation and are known for their stability [45, 46]. The variable step size for the adaptive time stepping size taken by the solver was informed by a prescribed absolute tolerance for the nonlinear solver and an implicit formulation of the mesh Courant-Friedrichs-Lewy (CFL) number. The solution sequence for the resulting systems of equations was fully-coupled in all dependent variables (fluid velocity and pressure, scalar concentration) for each solver iteration using an affine invariant form of the damped Newton method [47]. The nonlinear systems of equations were solved iteratively with specified convergence criteria using the restarted Generalized Minimum Residual (GMRES) solver [48, 49, 50], with the GCRO-DR method for Krylov subspace recycling [51] useful for solving sequences of linear systems arising from nonlinear equations. The solver was preconditioned with an algebraic multigrid (AMG) preconditioner [52], and consistent crosswind and streamline stabilization schemes were used for both fluid flow and scalar transport and diffusion. The discretization schemes and solvers detailed above, and implemented on the previously described mesh, yielded good numerical stability and solution convergence (discussed below) with acceptable memory and computation requirements. The dimensional model durations were constrained by the time required for a filament of streamwise width L_f introduced at the top boundary to advect at ambient flowspeed U_a through the PID suction distortion zone and out of the bottom boundary, thus capturing the full sequence of filament-suction interaction (Fig. 2a).

2.3.4. Model convergence and performance

We used several means of assessing the convergence and performance of the numerical model, relative to both fluid flow and scalar transport and diffusion. In addition to the traditional mesh refinement study detailed above, mesh convergence and numerical stability in the computation of the flow field were assessed through velocity profiles taken in the interior needle flow; this is the model region with the smallest length-scales, highest velocities, and strongest velocity gradients. The smoothness, monotonicity (when appropriate), and accuracy of these profiles relative to imposed flow boundary conditions at the outlet sensor location assured that the flowfield computation was well-converged and accurate across the parameter space tested (Table A.6). For scalar transport and diffusion, confirmation of expected peak concentration arrival time at the edge of the suction distortion zone based on the concentration boundary condition at the top boundary inlet for the given advection time, as well as corresponding diffusive pulse broadening measured over this time that closely matched analytical predictions (Eq. 16), indicated a converged and accurate scalar concentration field in space and time in the exterior flow. In the interior needle flow, highly refined mesh elements mitigate potential effects of high local Péclet number. Smooth and physical concentration pulse time records at the sensor level presented below indicate good convergence and accuracy for the scalar field in the interior flow. Finally, note that similar numerical methods to those employed here (meshing, discretization schemes, initial and boundary conditions, solvers) have been shown to accurately resolve the spatiotemporal dynamics of a pure suction flow field of similar suction Reynolds number Re_{U_S}, relative to particle image velocimetry (PIV, [53]) measurements of the same flow [54].

3. Results

We first look at the structure of the sampling flow field dictating the transport and dispersion of a scalar of interest (Eq. 11) during PID sampling from the farfield of the exterior flow to the sensor location far down the needle. We examine the effect of relative suction rate on the exterior flow (Figs. 5 and 6), as well as the effects of relative suction rate and suction Reynolds number on the interior needle flow (Fig. 8, Table 3). Then we quantify signal distortion (Figs. 9 and 10) across a large parameter space (Table A.6) and explore how the peak amplitude and pulse width ratios vary with three important nondimensional parameters: relative filament size, relative suction rate, and ambient Reynolds number (Figs. 11 and 12). Finally, we build

robust regressions capable of predicting distortion levels as a function of those key nondimensional parameters (Fig. 13, Table 4), providing PID users a means of estimating distortion levels and informing mitigation strategies.

3.1. PID sampling flowfields: exterior and interior flows

Axial profiles of normalized velocity magnitude are compared in Fig. 5 for the numerical model (green curves) and potential flow solution (blue curves, Eqn. 1), across relative suction rate U_s/U_a. The PID suction contribution to the overall spatial structure of the exterior flowfield often resembles the analytical point sink description predicting radially converging flow towards the orifice with a $1/r^2$ decay in suction velocity magnitude (Fig. 3). The profiles closely match in the farfield, including at the edge of the suction distortion zone at L_s/ϕ (half-width), but start to diverge closer to the orifice at $z^* = 0$. Here, the impermeability and no-slip conditions along the needle walls, along with the directional flow boundary condition at the orifice, are not resolved in the (inviscid and purely radial) potential flow description [25], which also becomes unbounded in the limit as $r \to 0$.

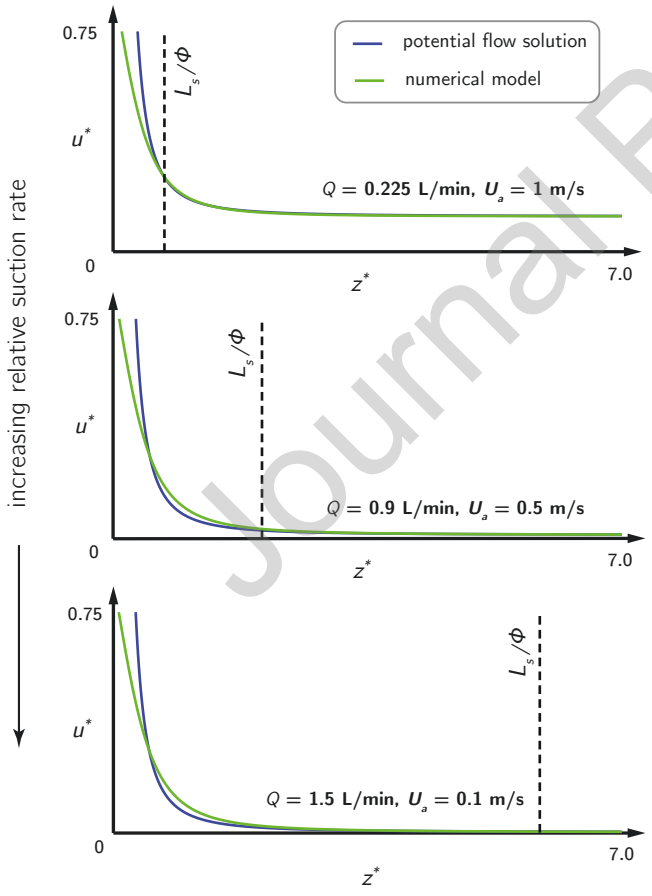

Figure 5: Axial profiles of normalized velocity magnitude ($u^* = u/U_s$) taken along the z-axis comparing the potential flow solution to the actual (modeled) flow field, for varying relative suction rates (increasing top-to-bottom panels). Note that the potential flow solution is a good descriptor of the modeled axial fluid velocities in the far-field, including up to the edge of the suction distortion zone, but fails near the orifice.

The accuracy of the potential flow description of the exterior PID sampling flowfield also breaks down with decreasing relative suction rate U_s/U_a, where the exterior flow converging towards the orifice becomes increasingly directional, biased towards the ambient flow direction since U_a is strong relative to the suction velocity U_s. The spatial structures of the exterior flowfield for varying relative suction rate in Fig. 6 illustrate this, where the ambient flow speed U_a increases in rows from top to bottom and the suction flowrate Q increases in columns from left to right. Thus, U_s/U_a varies from a minimum in the lower left corner to a maximum in the upper right. At low U_s/U_a, the pathlines denoting the (nondiffusive) fluid capture cone (computed from a standard set of starting points distributed along the orifice and integrated with the flow backward in time) collapse into a narrow streamtube with a diameter comparable to ϕ. The geometry of the suction distortion zone, denoted by the gray normalized velocity magnitude contour, becomes i. small relative to ϕ and ii. increasingly non-spherical, again being biased towards the ambient flow direction. As U_s/U_a increases, the fluid capture cone broadens with the increased relative strength of U_s, since a larger volume of fluid must pass through the orifice per unit time. This results in highly curved pathlines that rapidly converge to the orifice from the farfield. The geometry of the suction distortion zone also becomes large and increasingly spherical, since the suction flow with relative high U_s broadens the extent of the sink-like flow region near the orifice. For reference, the dependence of the (nondiffusive) fluid capture cone diameter L_{cc} on relative suction rate is shown in Fig. 7; the symbols correspond to the nine discrete cases from Fig. 6 and the dashed blue line is the least-squares best fit showing a $(U_s/U_a)^{0.5}$ dependency for capture cone diameter.

We also quantify the structure of the interior flow (Fig. 8), beginning at the orifice and extending downstream to the sensor, through radial profiles of normalized velocity magnitude. The entry (*inlet*) velocity profiles at the orifice (blue curves everywhere) are insensitive to both absolute and relative suction rate (U_s in Fig. 8a and U_s/U_a in 8b, respectively) here. All suction flowrates Q produce suction Reynolds numbers Re_{Us} (Table 3) that yield symmetric entry velocity profiles with a characteristic inversion near the needle centerline and near-wall maxima. This non-uniform profile has been previously observed in this range of Reynolds numbers ([25, 55, 56]) and influences the subsequent hydrodynamic development length as the entry profile spatially evolves downstream into the fully-developed laminar (Hagen-Poiseuille) pipe flow profile [57]. Regardless of the shape of the entry profile, the development length is a known function of suction Reynolds number (e.g., $= 0.075 Re_{U_s}$ [58]), such that PIDs sampling with different suction flowrates Q spatially develop differentially with distance downstream of the needle orifice. This is seen in the radial profiles in Fig. 8 taken at different distances downstream of the orifice. The transition from the entry profile (blue curve) to the fully developed profile (black parabolic profile) unfolds over different distances. Note that only the hypothetical low Q is fully-developed over the length of the needle, whereas the three standard Q of the 200B miniPID remain undeveloped (Table 3).

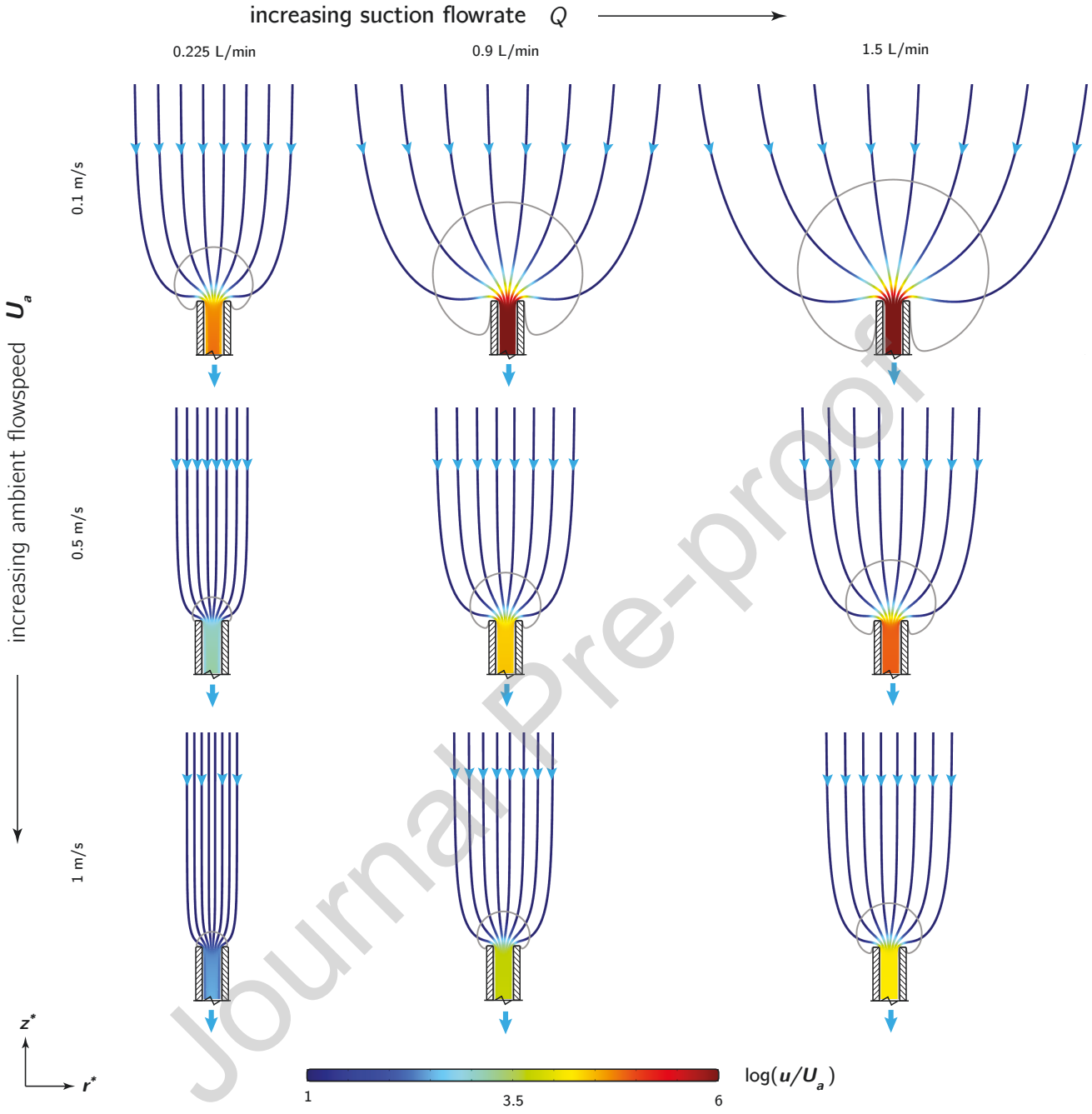

Figure 6: Fluid velocity fields for varying relative suction rates U_s/U_a (Q increases in columns from left-to-right and U_a increases in rows from top-to-bottom), represented through pathlines colored by normalized velocity magnitude (log-scale) and a gray contour line showing the extent of the suction distortion zone (L_s, normalized local velocity u/U_a equals two). The needle walls are denoted as black rectangles with cross-hatching. Note that the outermost pathlines in each panel denote an effective fluid *capture cone* delineating fluid volumes that are ultimately inhaled through the orifice versus those that remain exterior to, and ultimately bypass, the sampling needle.

3.2. PID sampling: idealized filament-suction interaction

The interaction of a diffusive scalar filament with the suction field of a sampling PID in time is illustrated Fig. 9, for a small relative filament size L_f/ϕ and intermediate-high relative suction rate U_s/U_a. As the filament approaches the PID needle orifice (Fig. 9a,b), the leading edge of the filament is deformed by the suction distortion field along the axis of the needle where the ambient and suction velocities are aligned, causing the filament to accelerate towards the orifice and stretching the interface between the scalar and ambient fluid. As the filament is further advected towards the orifice (Fig. 9c), it may split as ambient fluid is drawn along the axis of the needle and penetrates the filament from behind along the trailing edge (upstream side). Finally, as the filament passes out of the suction distortion zone

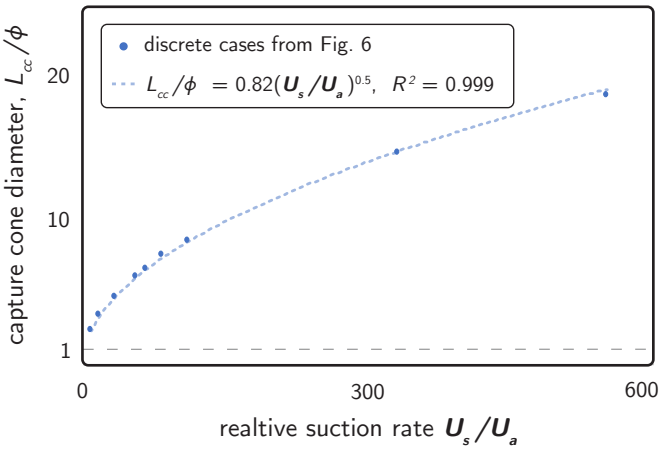

Figure 7: Diameter of the nondiffusive fluid capture cone L_{cc} (normalized by the needle diameter ϕ) as a function of relative suction rate U_s/U_a. The symbols correspond to the nine discrete cases from Fig. 6 and the dashed blue line is the least-squares best fit showing a $(U_s/U_a)^{0.5}$ dependency for capture cone diameter.

Table 3: Nondimensional flow development lengths as a function of suction Reynolds number Re_{U_s} for a hypothetical, ultra-low suction flowrate, as well as the three standard to the Aurora Scientific 200B miniPID. Across the resulting range of Re_{U_s}, the shape of the entry flow profiles at the orifice are nearly identical. However, the resulting spatial development of the interior flow, as the entry flow profile approaches the Hagen-Poiseuille laminar pipe flow profile over the flow development length, differs notably. Note that the nondimensional development length reported here ($= 0.075 Re_{U_s}$) is taken from [58]; other more recent formulations exist (e.g., [59, 60]) and yield negligible differences in the predicted development length. Note also that only the ultra-low hypothetical Q is hydrodynamically fully-developed over the PID needle length ($z/L_n = 1$).

Q [L/min]	Re_{U_s}	development length $[z/\phi]$	development length $[z/L_n]$
0.225	425	31.9	0.43
0.9	1700	127	1.70
1.2	2270	170	2.3
1.5	2840	212	2.8

(Fig. 9d), the trailing edge near the orifice is similarly distorted in regions of the filament that are still in the fluid capture cone of the PID (Fig. 6). The exact nature of filament-suction interaction depends on the nondimensional parameters describing the sampling scenario; however, the sequence of Fig. 9 illustrates the key features of a distorting interaction.

3.3. PID distortion: peak amplitude and pulse width ratios

In Fig. 10a, we show how distortion levels vary across relative suction rate (increasing diagonally from lower-left to upper-right) for a fixed filament size $L_f = 2$ mm, by comparing the measured scalar concentration timeseries at the PID sensor (*sensed*, red curves) to that registered by an ideal probe in the absence of distorting effects (*undistorted*, green curve). The small relative filament size here dictates that these are generally cases with appreciable distortion levels, while the larger relative filament size in Fig. 10b illustrates additional nondistorting regimes. Key distorting features include not only modification

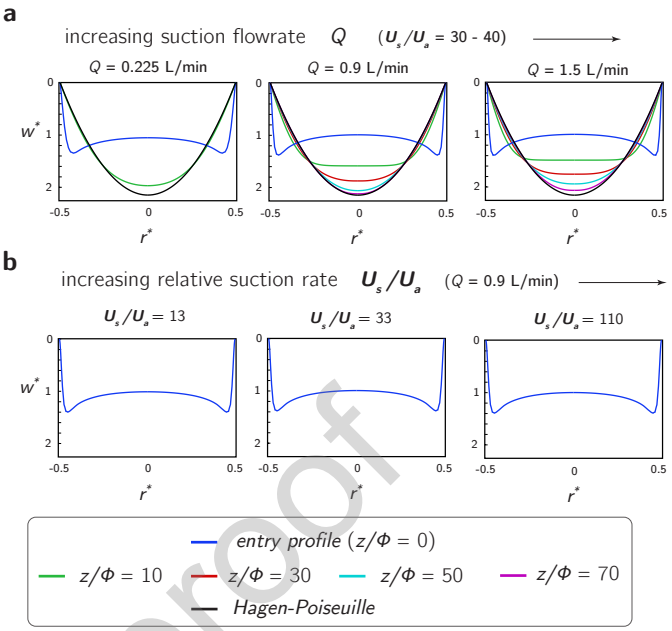

Figure 8: **a** Radial profiles of axial velocity in the interior needle pipe flow showing the effects of absolute suction flowrate Q for a small range of relative suction rates U_s/U_a on the entry (orifice) velocity profile (blue lines) and subsequent spatial development of the interior flow profile (colored lines) towards the fully-developed Hagen-Poiseuille laminar pipe flow profile (black line). **b** Radial profiles of axial velocity in the interior needle pipe flow showing the effects of relative suction rate U_s/U_a for a fixed absolute suction flowrate Q on the entry (orifice) velocity profile (blue lines).

to the peak arrival time and pulse attenuation (reduction of peak amplitude and broadening), but also potentially higher-order effects related to skewness and kurtosis. As described above, we focus on the peak amplitude ratio c_p^* and pulse width ratio σ^* (sensed-to-distorted values) as two informative distortion metrics characterizing pulse attenuation (Fig. 4).

3.4. Distortion scaling relationships

To effectively explore the distortion parameter space and gain insights into what mechanisms drive PID sampling distortion, we plot c_p^* and σ^* against two important timescale ratios in Figs. 11 and 12. In the top row of both figures, the timescale ratio on the horizontal axis is T_{Ls}/T_{Lf}, the time required for a point or feature to pass through the suction distortion field relative to the time required for a scalar filament to pass through a point in space. This effectively describes the relative importance of L_s versus L_f in the total filament residence time in the suction distortion field (Eqn. 6). In the bottom row, the timescale ratio on the horizontal axis is T_{Ls}/T_{Ln}, the time required for a point or feature to pass through the suction distortion filed relative to the residence time in the interior needle flow (orifice-to-sensor). Conceptually, these timescales might correlate to distorting effects arising in the exterior flow region versus those originating in the entry and interior flow regions. Their ratio would then indicate the relative strength of each and might effectively delineate distortion regimes with potentially unique physics and scaling in the relevant nondimensional parameters (discussed in detail below). In columns from left-to-right, data

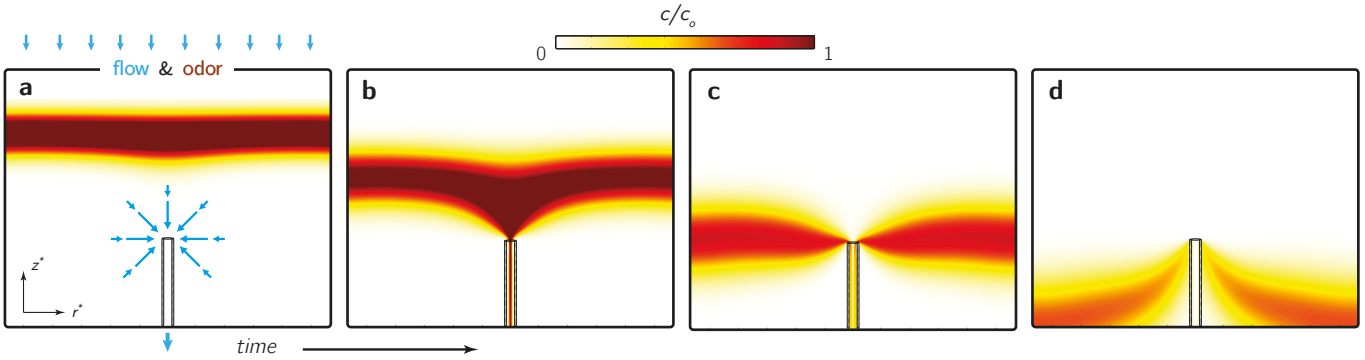

Figure 9: A representative time progression of source-normalized scalar concentration fields (contours) showing suction distortion as a filament is advected with the ambient flow (from top-to-bottom in each panel) towards an actively sampling PID needle. The time-resolved fluid velocity fields in both the exterior and interior flow regions, including the needle entry flow, capture multiple potential filament distortion mechanisms arising from the farfield of the exterior flow to the sensor.

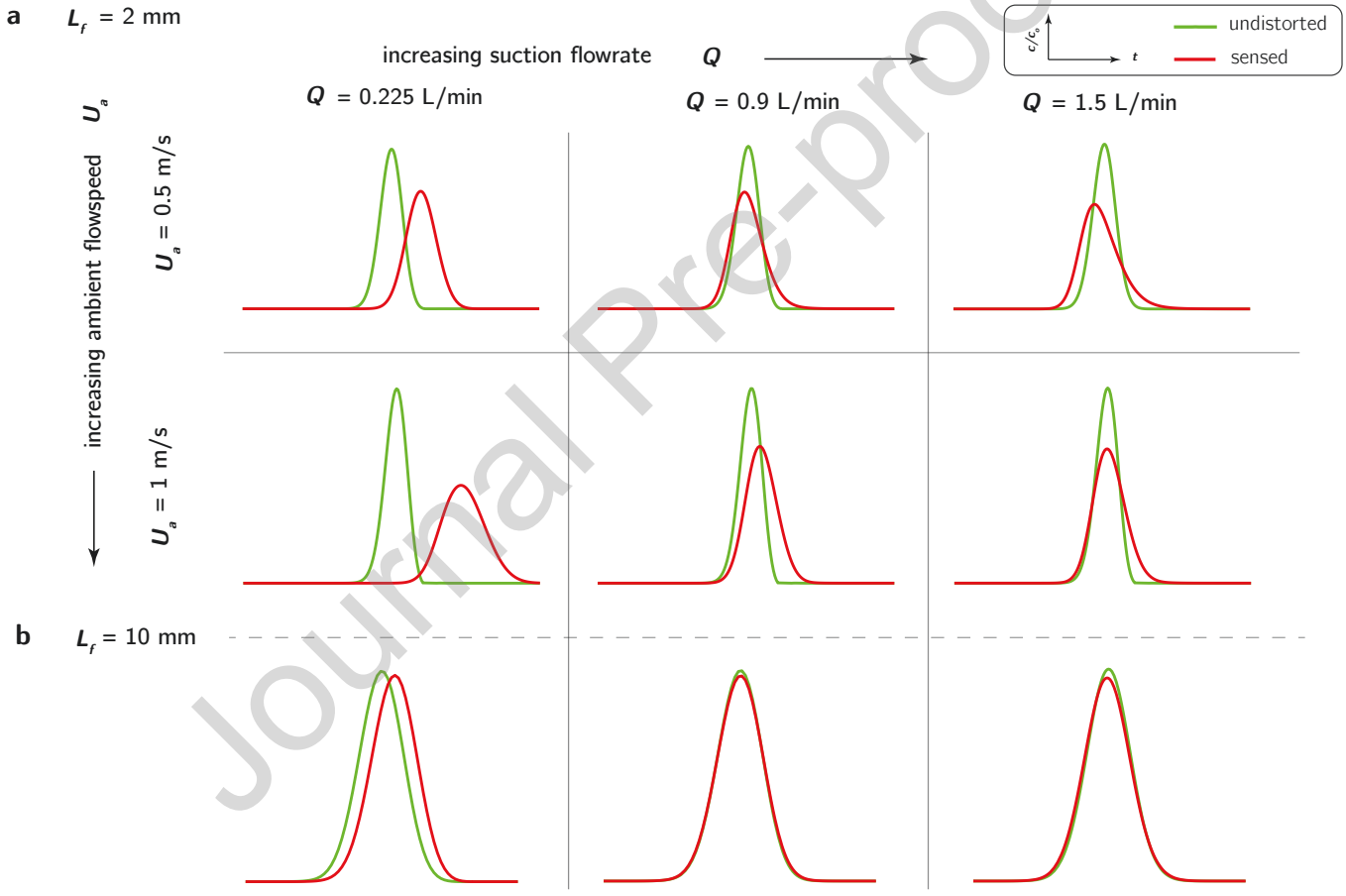

Figure 10: Undistorted (green lines) versus sensed (red lines) scalar concentration pulses registered in time for **a** L_f = 2 mm and **b** L_f = 10 mm. Suction flowrate Q increases in columns from left-to-right, and ambient flow speed U_a increases in rows from top-to-bottom in **a** and is constant (0.5 m/s) in **b**. Note the diversity of distortion effects represented in terms of nondimensional peak amplitude and pulse width ratios, peak arrival time, and skewness.

points are colored by each of those three important nondimensional parameters identified as likely to explain observed variations in distortion levels observed across the modeled parameter space: relative filament size ϕ/L_f (inverted), relative suction rate U_s/U_a, and the ambient flow Reynolds number Re_{Ua} (left-to-right columns, respectively).

We note several important findings from this exploration of the distortion parameter space. First, distortion varies systematically as a function of each nondimensional parameter: i. loose grouping by ϕ/L_f (left column) where distortion increases with decreasing filament size L_f, ii. increased distortion with both decreasing and increasing relative suction rate U_s/U_a (middle column) around some global distortion minimum within a given L_f group (more sensitive to decreasing U_s/U_a), and iii. weakly

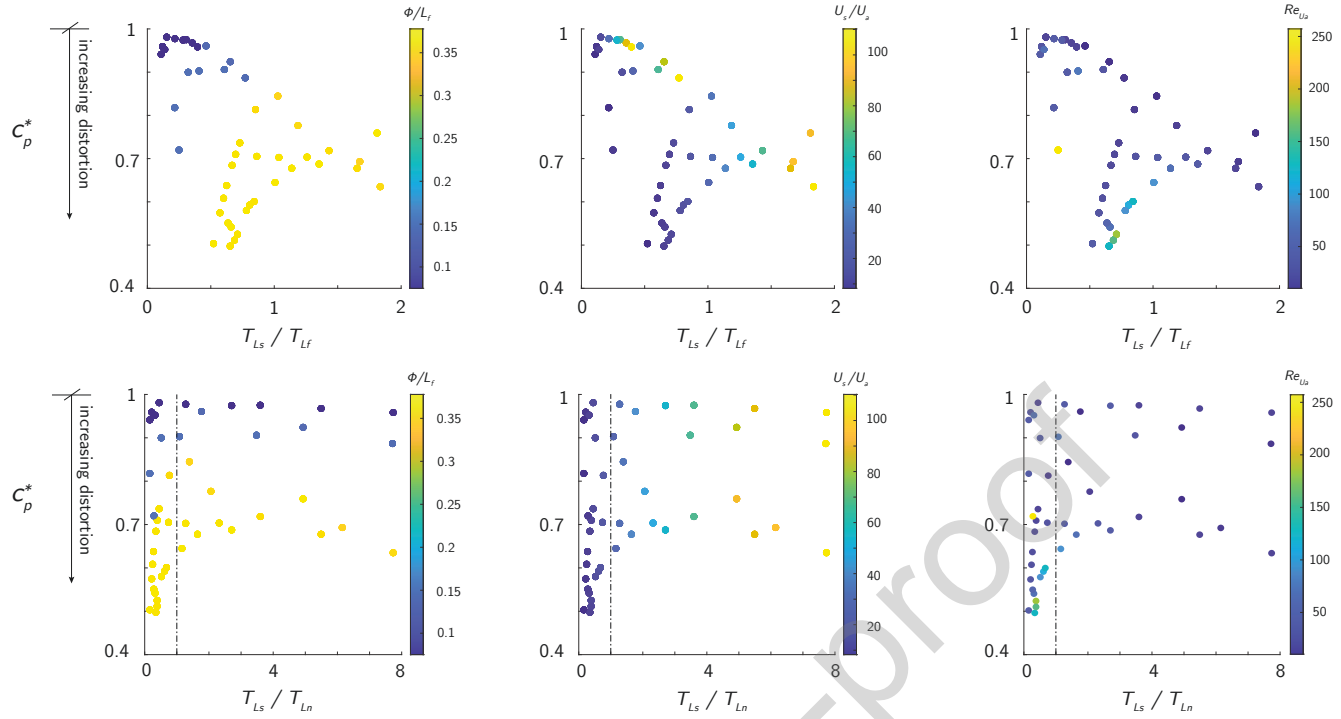

Figure 11: Exploration of variations in peak amplitude ratio c_p^* as a function of important timescale ratios, across the relevant nondimensional parameters (left column = relative filament size ϕ/L_f, middle column = relative suction rate U_s/U_a, right column = ambient Reynolds number Re_{U_a}). Top row: c_p^* versus the ratio of the distortion zone advection timescale T_{L_s} to the filament advection timescale T_{L_f}. Bottom row: c_p^* versus the ratio of the distortion zone advection timescale T_{L_s} to the needle residence time T_{L_n}. Note the systematic variation in distortion as a function of each nondimensional parameter, the existence of non-monotonic behavior in distortion versus each timescale ratio, and the evidence for a global, ideal relative suction rate that minimizes distortion across all filament sizes (e.g. vertical dashed black line in bottom row).

increasing distortion with increasing ambient Reynolds number Re_{Ua} (right column) for a given L_f. Second, there is clear evidence for non-monotonic behavior in distortion scaling across the parameter space (parabola-shaped distortion curves within L_f groups in the top row), potentially delineating unique distortion regimes driven by different mechanisms (with the breakpoint at the timescale ratio equal to 1, vertical dashed black line in bottom row). Last, there is a possible ideal relative suction rate U_s/U_a that minimizes distortion across all filament sizes (L_f) and ambient flow speeds (U_a) with proper scaling in the relevant nondimensional parameters, given the systematic variations in each parameter described in detail above.

The insights gained from the exploration of the distortion parameter space in Figs. 11 and 12 are distilled into a single distortion scaling relationship described by Eqns. 17 and 18 and shown in Fig. 13. The nondimensional distortion scaling parameter S_D (introduced and described below) describes PID geometry and sampling conditions and is used to build regression relationships that are capable of predicting distortion levels to a high degree of accuracy and confidence. The regressions for measured distortion level (c_p^* in Fig. 13a and σ^* in 13b) as a function of the predicted scaling parameter S_D are linear as follows,

$$c_p^* \text{ or } \sigma^* = mS_D + b \,, \tag{17}$$

where S_D is the product of three functions, each varying in one of the relevant nondimensional parameters ϕ/L_f,U_s/U_a, and Re_{Ua} as

$$S_D = \frac{\phi}{L_f}\left[\frac{2}{(U_s/U_a)^{1/2}} + \frac{1}{225}\frac{U_s}{U_a}\right]\log_{10}(\mathrm{Re}_{Ua}) \,. \tag{18}$$

The process of selecting the specific functional form for each nondimensional parameter's contribution to S_D was somewhat *ad hoc*, but was strongly informed both by the insights gained from exploring the distortion parameter space in Figs. 11 and 12 (discussed in detail above) and the suction distortion zone lengthscale previously introduced, L_s. The basic approach was as follows:

- Begin with simple functional forms (e.g., linear form for relative filament size) that accurately reflect distortion variations in each nondimensional parameter
- Add functional complexity as required (e.g., nonlinear, non-monotonic, two-term form for relative suction rate)
- Assess the performance of the full distortion scaling parameter S_D in its explanatory power for measured distortion
- Maintain a slope (Eqns. 17) on the order of one, such that functional forms and terms are likely to have some physical significance
- Iterate and maximize the distortion scaling model (Eqns. 17 and 18) coefficient of determination R^2

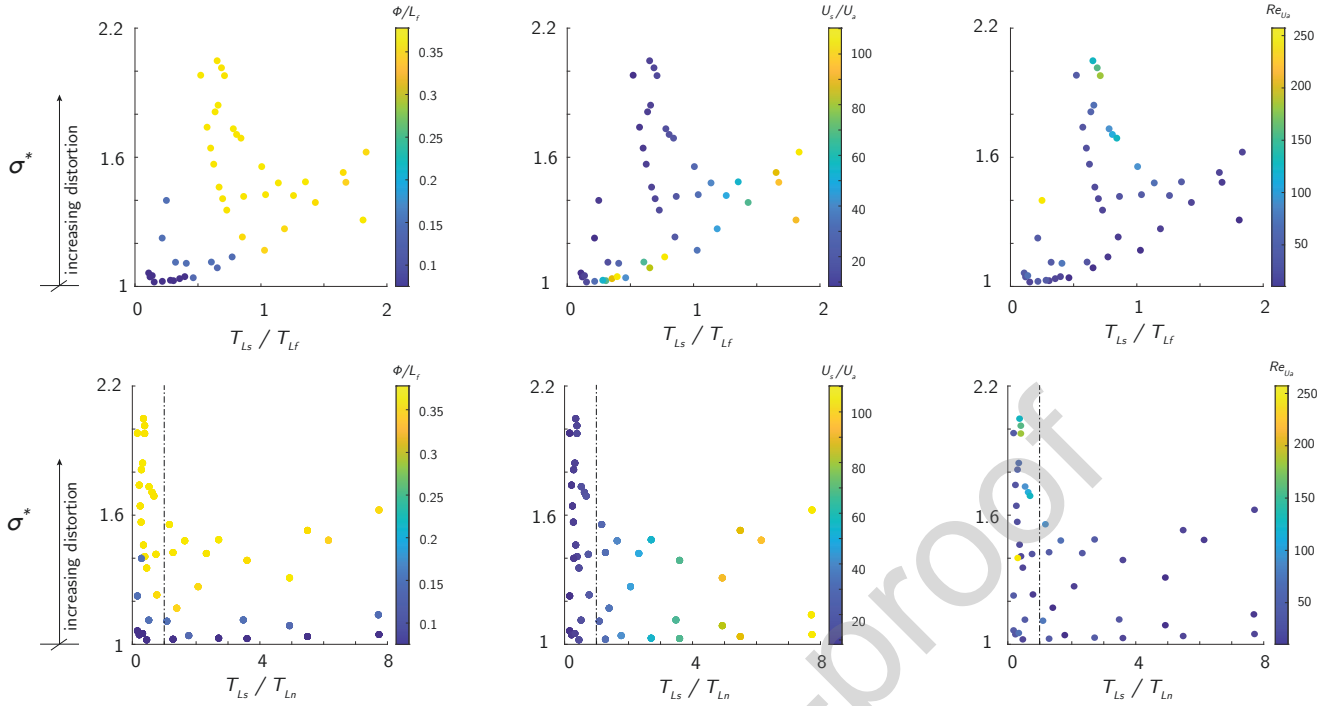

Figure 12: Exploration of variations in peak amplitude ratio σ^* as a function of important timescale ratios, across the relevant nondimensional parameters (left column = relative filament size ϕ/L_f, middle column = relative suction rate U_s/U_a, right column = ambient Reynolds number Re_{U_a}). Top row: σ^* versus the ratio of the distortion zone advection timescale T_{L_s} to the filament advection timescale T_{L_f}. Bottom row: σ^* versus the ratio of the distortion zone advection timescale T_{L_s} to the needle residence time T_{L_n}. While variations in pulse width ratios across the important nondimensional parameters broadly mirror those in the peak amplitude ratio c_p^* in Fig. 11, the two are not redundant since they are not explicitly coupled, for example, by a constraint of scalar mass conservation in the undistorted and sensed pulses.

The columns from left-to-right in Fig. 13 show progressive products of these functions leading to the full distortion scaling parameter S_D in the right column, illustrating the role of each in explaining the variability in observed distortion levels and in collapsing the data along the expected scaling curve. Measured distortion is plotted against S_D in the right column, along with the linear least squares regression prediction (solid red line) and 95% confidence interval (dashed red lines). Note that scaling distortion by the products of functions of the individual relevant nondimensional parameters, as done here, is equivalent to an assumption of linearity in their respective contributions to distortion.

Table 4: Summary of model fit parameters for distortion (c_p^* or σ^*) as a function of the scaling parameter $S_D = (\phi/L_f)\,[2/(U_s/U_a)^{1/2}+(U_s/U_a)/225]\log(Re_{U_a})$.

distortion metric	slope (m)	y-intercept (b)	R^2
c_p^*	-1.170	1.05	0.988
σ^*	2.260	0.828	0.942

The distortion scaling parameter S_D (Eqn. 18) accounts for the total variability observed in distortion levels across the model parameter space remarkably well (R^2 = 0.988 and 0.942 for c_p^* and σ^*, respectively). The robust fit offers some confirmation of the appropriateness of the functional form selected for distortion sensitivity in each nondimensional parameter. Those functional forms are linear in relative filament size ϕ/L_f, nonlinear but monotonic in ambient Reynolds number ($\log_{10} Re_{Ua}$), and nonlinear and non-monotonic for relative suction rate U_s/U_a. The U_s/U_a function consists of two terms. One term decays with the root of U_s/U_a, and the other grows linearly, albeit slowly, with U_s/U_a. Several important insights arising from this non-monotonic distortion scaling, and more generally the functional forms of each parameter's distortion dependence, are commented on throughout the discussion below. Note that for simplicity of presentation here both distortion metrics in Fig. 13 are fit to a single form of S_D (Eqn. 18); however, alternate forms for σ^*—e.g., a weakly nonlinear contribution for ϕ/L_f with a power of 3/4—slightly improve the distortion model fit for this higher-order metric. Optimizing the form of S_D for c_p^* and σ^* independently is beyond the scope of work here, especially considering the remarkable predictive power of S_D (Eqn. 18) for both metrics (Table 4).

In the following case study we apply the distortion model presented above (Eqns. 17-18, Table 4) to predict and evaluate distortion levels when sampling a real plume across a range of hypothetical, user-adjustable suction velocities U_s. The ensuing discussion highlights numerous points of interest to PID users interested in our findings, including specification of the minimum acceptable values of the distortion scaling parameter S_D required for application of our distortion model. For values of S_D below this threshold our model predicts nonphysical dis-

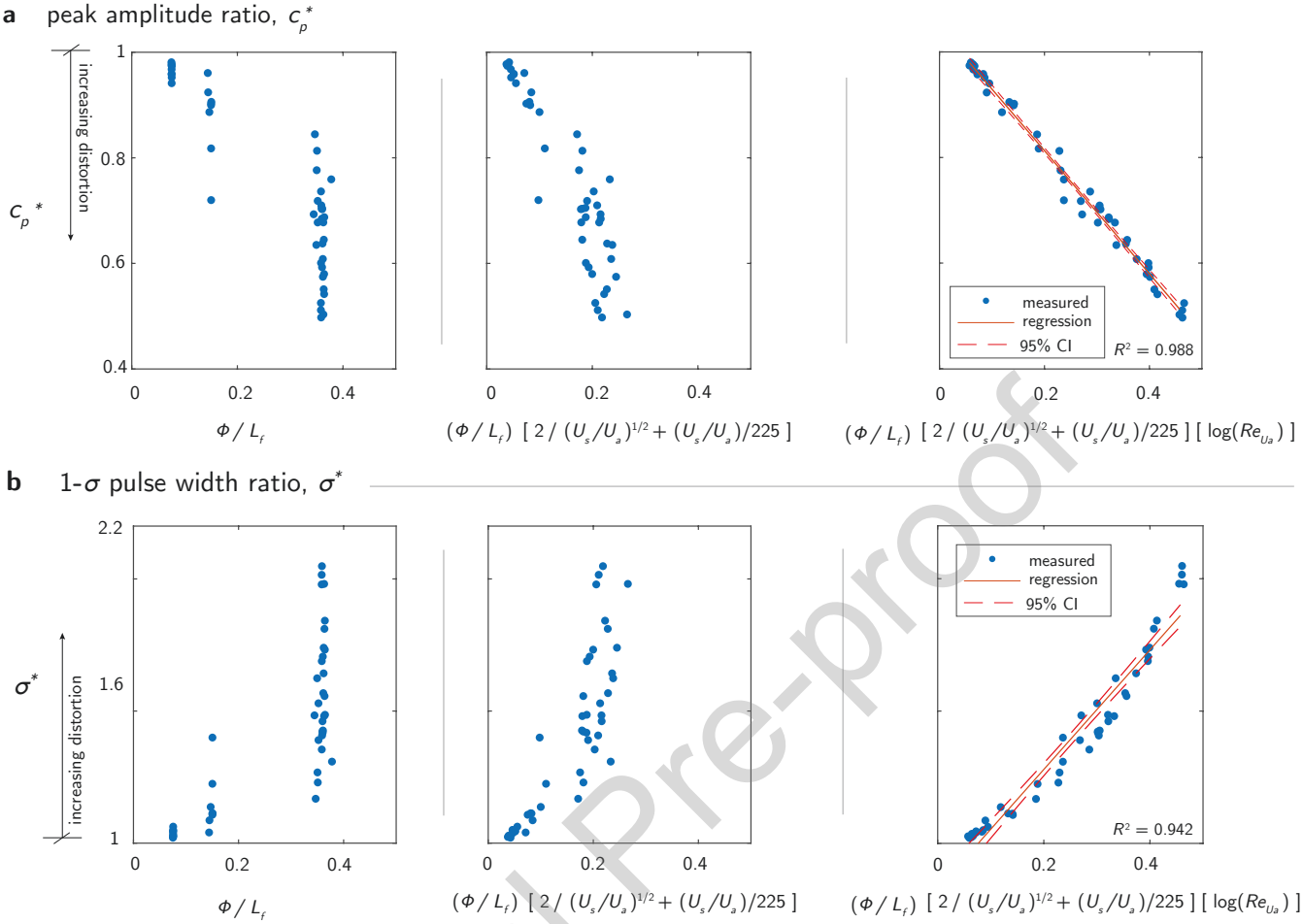

Figure 13: Distortion scaling versus progressive products of functions of each relevant nondimensional parameter for **a.** peak amplitude ratio c_p^* and **b.** pulse width ratio σ^*. Distortion levels are plotted against ϕ/L_f (left column), $(\phi/L_f)\ [2/(U_s/U_a)^{1/2} + (U_s/U_a)/225]$ (middle column), and the full distortion scaling parameter $S_D = (\phi/L_f)\ [2/(U_s/U_a)^{1/2} + (U_s/U_a)/225]\log(Re_{U_a})$ (right column). The progression shows the effect of each nondimensional parameter in collapsing the measured (modeled) distortion data onto the predicted scaling curve. A linear least-squares regression of distortion as a function of the final distortion scaling parameter S_D yields an excellent fit that captures almost all observed variability (right column). The regression provides an empirical, closed-form predictor for distortion as function of PID geometric and operational parameters.

tortion behaviors (towards the limit of zero-distortion), and for values above the threshold the model predicts measured distortion levels robustly for a range of realistic plume and sampling conditions (Fig. 13).

3.5. Case study in a real plume: predicting distortion levels and selecting an optimal sampling suction velocity

To highlight the significance and usefulness of our findings to PID users, we explore a case study from [5]. We aim to illustrate the process of i. identifying individual scalar filament structures in measured plume time series data, ii. estimating the expected levels of signal distortion (peak amplitude and pulse width ratios) under hypothetical PID sampling with the Aurora Scientific miniPID (200B) in the given plume environment, and iii. tuning suction velocity U_s for minimization of distortion, as well as estimation of residual distortion levels that persist under optimal sampling conditions. We explore different aspects of this sequence in detail in the discussion below and the results are summarized in Fig. 14.

The instantaneous scalar concentration field shown in Fig. 14a is representative of the spatiotemporal structure of the odor landscape produced by a low-speed gaseous plume. The contours show the source-normalized concentration field produced by a neutrally-buoyant plume of acetone vapor emanating isokinetically (at the same speed as the mean ambient flow) from a round tube (1 cm inner diameter) into a low-speed (ambient flowspeed U_a = 0.2 m/s) wind tunnel flow with weak grid turbulence. The plume was quantified using planar laser-induced fluorescence (PLIF) with 15 Hz resolution and is described in [5]. For illustrative purposes here, we examine a one-minute concentration time series from the PLIF data (Fig. 14b), representing the undistorted signal registered by an ideal (nondistorting) probe sampling in this plume environment. We then show how a PID user can apply the distortion parameterization provided herein to i. estimate the expected levels of signal distortion produced during sampling with the Aurora Scientific miniPID and/or ii. identify how distortion levels vary with user-tunable suction velocity U_s, including at the optimal distortion-

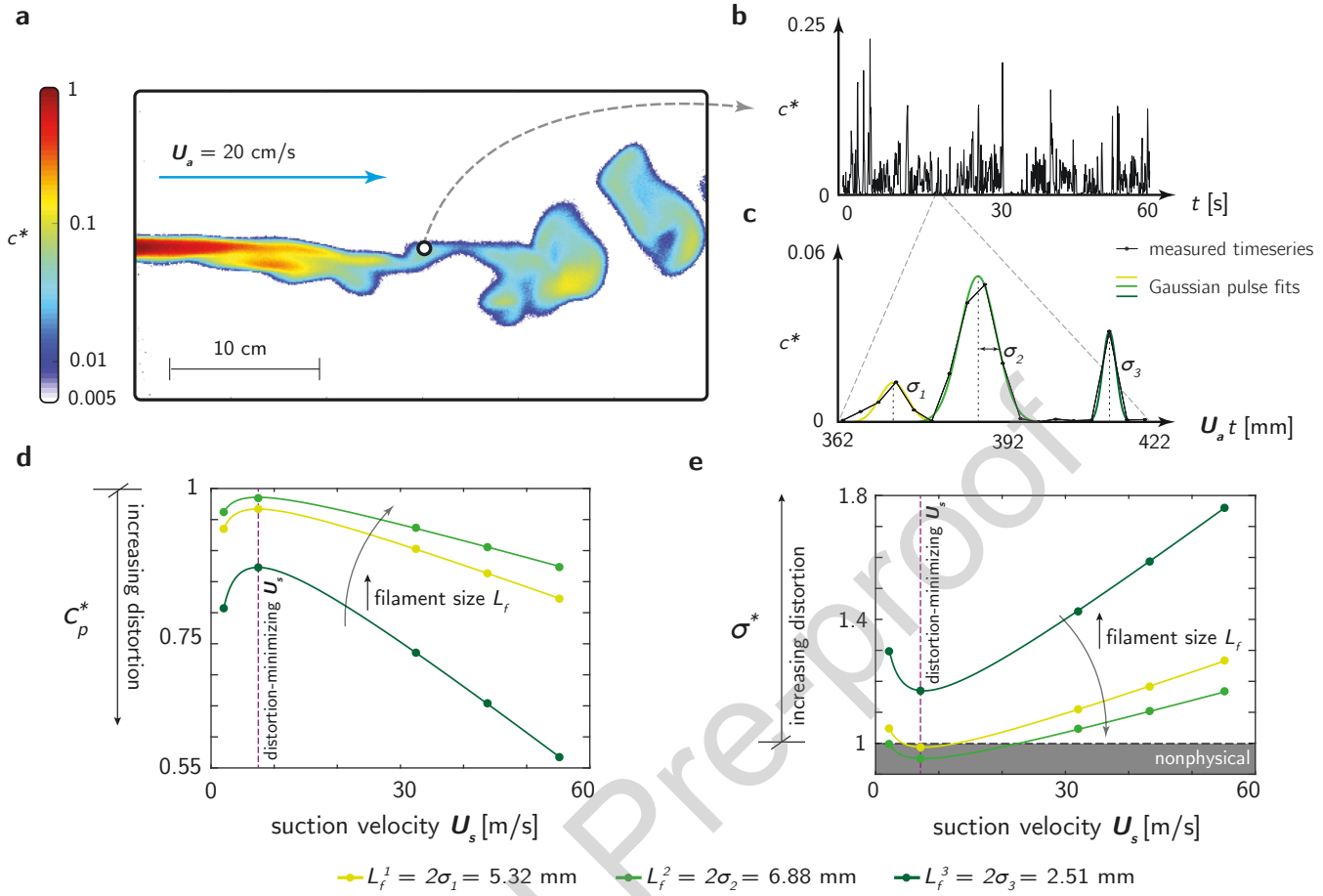

Figure 14: Case study illustrating how to estimate signal distortion levels in a given plume sampling application and how to select a distortion-minimizing suction velocity U_s. **a.** An instantaneous, source-normalized concentration field (contours) produced by a neutrally-buoyant plume in a low-speed wind tunnel flow. **b.** A one minute concentration time series taken on the plume centerline 15 cm downstream of the source. **c.** A real sequence of three odor pulses registered at the measurement point in the previous time series, including the raw concentration time series (black line with symbols) and a best Gaussian fit to each pulse (curves in shades of green), plotted against the corresponding space dimension $U_a t$ (see text). **d.** The predicted peak amplitude ratio c_p^* of each filament (individual curves with dots in shades of green) comprising the odor pulse train in **c.**, as a function of hypothetical suction velocity U_s. The individual dots on each curve represent discrete sampling suction velocities U_s (and thus U_s/U_a) selectable by a PID user. The corresponding relative suction rates U_s/U_a at each dot from left to right represent a hypothetical low $U_s/U_a = 10$ (far left), the ideal distortion-minimizing $U_s/U_a = 35$ (dashed purple line), and the three standard U_s/U_a produced by the 200B miniPID (Table 1) when sampling in this plume with $U_a = 0.2$ m/s. **e.** The predicted pulse width ratio σ^* of each filament (individual curves with dots in shades of green) comprising the odor pulse train in **c.**, computed and presented as in **d.**. See text for explanation of the nonphysical region denoted by the shaded rectangle.

minimizing U_s corresponding to an ideal relative suction rate U_s/U_a of 35 (see Discussion section). Note that if we alternatively had considered the time series of Fig. 14b as a hypothetical *distorted* signal registered by a PID (i.e. the situation when the undistorted signal is not known *a priori*), we could algebraically manipulate the distortion equations (Eqns. 13-14, Eqns. 17-18, Table 4) to setup up a system of equations to solve for the true (undistorted) peak amplitudes and pulse widths.

The process of identifying individual scalar filament structures of varying spatial sizes registered by a point sensor (PID) in time is shown in Fig. 14c and involves the invocation of Taylor's *frozen turbulence hypothesis*. The hypothesis states that the spatial structure of an entity of interest (e.g. a turbulent eddy or a scalar filament) is effectively unchanged as it advects with the mean ambient flowspeed U_a past a point sensor (as constrained by the relative magnitudes of the entity's travel time past the probe and a relevant dynamic timescale describing its evolution). The result is that the spatial structure of the entity of interest is deterministically mapped into the time series registered by the sensor through a simple variable transformation, where time t and space are related as $U_a t$. A representative odor pulse train extracted from the time series in Fig. 14b is shown in Fig. 14c, where the time axis has been mapped to its corresponding space dimension ($U_a t$), such that a Gaussian fit in space of the three pulses registered by the sensor in time yields the corresponding 2σ filament sizes L_f (undistorted). The three filaments comprising the pulse train are all sub-centimeter in size ($L_f^1 = 5.32$ mm, $L_f^2 = 6.88$ mm, $L_f^3 = 2.51$ mm) and thus, broadly speaking, we expect that distortion levels may be non-negligible (see Discussion section).

Once individual filament structures are identified in the measured PID concentration time series, and their corresponding

spatial sizes L_f are computed, one can compute the expected distortion levels (peak amplitude and pulse width ratios, c_p^* and σ^*, respectively, Eqns. 13 and 14, Fig. 4) as a function of the relevant sampling parameters describing PID geometry (needle inner diameter ϕ = 0.76 mm for the Aurora Scientific 200B miniPID, Table 1), filament size (L_f), ambient flowspeed (U_a = 0.2 m/s), and suction velocity U_s (corresponding to the volumetric suction flowrate Q and tunable by PID users, Eqn. 2). First, the dimensionless distortion scaling parameter S_D is computed (Eqn. 18), which is the product of three individual functions each with dependence on a single important nondimensional parameter (Table 2). The important nondimensional parameters include the relative filament size ϕ/L_f, the relative suction rate U_s/U_a (Fig. 3), and the Reynolds number based on the ambient flowspeed Re_{Ua} (Eqn. 10). Next, the linear distortion regression relationships (Eqn. 17, Table 4) are used to compute the magnitude of predicted distortion levels. In practice, the plume will have been sampled by the PID operating at a single discrete suction velocity U_s. However, for illustrative purposes here we varied U_s and computed the expected distortion levels to show how these levels vary as a PID user hypothetically samples the plume at different U_s. Predicted distortion levels across a range of realistic suction velocities are shown for each of the three filaments comprising the identified odor pulse train (Fig. 14c) in Fig. 14d-e (peak amplitude and pulse width ratios, c_p^* and σ^*, respectively).

Here, we discuss some key aspects of the predicted distortion curves of Fig. 14d-e, while providing more detailed insights into distortion scaling and regression relationships in the Discussion section below. First, all sampled filaments here are subject to appreciable distortions levels (≈ 5 - 45% reduction in peak amplitude and up to almost 80% increase in pulse width), and smaller filaments experience both higher distortion overall as well as increased sensitivity to variations in suction velocity U_s. Next, for all filament sizes there exists a global optimal suction velocity U_s that minimizes signal distortion and corresponds to an ideal relative suction rate U_s/U_a = 35; however, some residual distortion may always exist even under optimal sampling conditions. Last, for some combinations of L_f and U_s/U_a the regression relationship for σ^* predicts nonphysical effects corresponding to $\sigma^* < 1$ as indicated by the rectangular shaded region in Fig. 14e. This region is nonphysical since it predicts distorted (sensed) filaments with widths L_f smaller than the undistorted filament widths. While not the case here, note that the peak amplitude ratio regression may also predict nonphysical effects with $c_p^* > 1$ corresponding to distorted (sensed) peak amplitudes larger than undistorted amplitudes. This highlights the importance of applying the distortion model herein only for applicable values of the scaling parameter S_D, namely only for values of S_D greater than the x-intercept (i.e. S_D) at y (i.e. c_p^* or σ^*) = 1 in the linear distortion regressions of Fig. 13. The corresponding minimum cutoff values for S_D, below which the regressions predict nonphysical distortion behavior as in the portions of the curves in the shaded nonphysical region of Fig. 14e, are thus 0.0427 and 0.0761 for c_p^* and σ^*, respectively. Small S_D values (i.e. distortion levels) can be driven most notably by large filament sizes L_f and small ambient velocities U_a (Eqn. 18).

Finally, to help give PID users intuition about what parameters drive distortion and what resulting distortion levels might be dimensionally, we computed distortion for several hypothetical cases while holding key parameters constant using the prediction model provided herein (Eqns. 17-18, Table 4). These results are summarized in Table 5 and for three filaments (L_f = 2, 5, and 10 mm) being sampled by an Aurora Scientific 200B miniPID at three different suction velocities U_s (standard suction rates on 200B) in two plume environments (U_a = 0.2 m/s in upper group, 2 m/s in lower group). For a given sampler, distortion increases with higher U_a for a fixed L_f and U_s (upper group versus lower group). For fixed U_a, distortion levels decrease with increasing U_s to a point, reaching their minimum values at the optimal U_s corresponding to the ideal U_s/U_a = 35 (more in the Discussion section below), and subsequently increase with increasing U_s (e.g. trends in the L_f = 2 mm group of the upper and lower table groups). Lastly, smaller filaments are more subject to distortion for fixed U_s and U_a.

Table 5: Predicted distortion for the Aurora Scientific 200B miniPID across a range of parameters including ambient flowspeed U_a (top group at 0.2 m/s, bottom group at 2 m/s), filament size L_f, and suction velocity U_s (three standard suction rates). The bottom three rows show predicted distortion levels when sampling the 2 m/s plume at the optimal suction velocity of 70 m/s (corresponding to an ideal relative suction rate U_s/U_a of 35). *Case where scaling parameter S_D is below minimum threshold for application of the distortion prediction model resulting in nonphysical distortion predictions. Note that the distortion metrics in the last two columns on the right are related to the peak amplitude and pulse width ratios as (1-c_p^*) x 100 and (σ^*-1) x 100.

U_a = 0.2 m/s

L_f [mm]	U_s [m/s]	S_D	% reduction in amplitude	% increase in pulse width
2	33.065	0.342	35.04	60.15
2	44.087	0.428	45.12	79.62
2	55.109	0.517	55.50	99.66
5	33.065	0.137	11.02	13.74
5	44.087	0.171	15.05	21.53
5	55.109	0.207	19.20	29.54
10	33.065	0.068	3.01	−1.73*
10	44.087	0.086	5.02	2.16
10	55.109	0.103	7.10	6.17

U_a = 2 m/s

L_f [mm]	U_s [m/s]	S_D	% reduction in amplitude	% increase in pulse width
2	33.065	0.432	45.56	80.47
2	44.087	0.401	41.86	73.31
2	55.109	0.385	40.03	69.78
5	33.065	0.173	15.23	21.87
5	44.087	0.160	13.74	19.01
5	55.109	0.154	13.01	17.59
10	33.065	0.086	5.11	2.33
10	44.087	0.080	4.37	0.90
10	55.109	0.077	4.01	0.20
2	70	0.377	39.15	68.07
5	70	0.151	12.66	16.91
10	70	0.075	3.83	−0.15*

4. Discussion

Considering the spatiotemporal structure of the PID sampling flowfield, from the farfield of the exterior flow away from the orifice to the interior needle flow leading to the sensor, distorting effects may arise from a variety of origins. These include the suction distortion field from PID suction, pure ambient flow effects related to the presence of the needle, the entry flow region where the exterior flow transitions around and through the orifice to the interior needle flow, and pipe flow dispersion effects. Dispersion effects could originate during flow development as the interior pipe flow profile spatially evolves from that at the orifice to the fully-developed laminar profile (Hagen-Poiseuille flow) downstream [57]) or from (fully-developed) laminar dispersion (shear dispersion) en route to the sensor [42]. Distorting effects arising in the exterior regions of the flow may be due simply to mixing of scalar-dosed and ambient fluid when the scalar-fluid interface is drawn preferentially along the needle axis as the filament approaches the suction distortion field (Fig. 9). Distorting effects everywhere may also arise from a higher-order mechanism related to flow-enhanced diffusivity as the local deformation (velocity gradient) field strains mass-conserving scalar filament structures; this is analogous to turbulent diffusion in which macroscopic stirring enhances concentration gradients through filament straining, which in turn enhances local scalar concentration gradients and drives enhanced molecular diffusion (see turbulence discussion below).

The potential relevance of different distortion mechanisms can be surmised by looking at the values (ratios) of several important advective and diffusive timescales. For the parameter space covered in the model runs here (Table A.6), which includes both distorting and non-distorting regimes, these timescale ratios indicate simple mixing (either in the exterior approach to the needle or at the sensor/ionization chamber level) as described above being the most likely predominant distortion mechanism since the scalar molecular diffusion timescale ($T_D = \phi^2/D = 46.6$ ms) is usually an order of magnitude longer than, for example, the total capture time required to pass through the suction distortion zone and down the needle ($\approx T_{Ln} + L_s/U_s$, ranging from 1.05 to 7.04 ms here). Flow-enhanced diffusion may also be potentially relevant for some distorting cases when the distortion zone advection timescale T_{Ls} (Eqn. 4, ranging from 0.25 ms to 15.3 ms here) becomes long relative to the scalar diffusion timescale T_D. Additionally, since the tube residence time T_{Ln} (ranging from 1.03 - 6.90 ms for the four Q modeled) is comparable to or longer than the radial homogenization time predicted by Taylor [42] ($T_{\phi_o} = (\phi/2/3.8)^2/D = 0.81$ ms), it seems likely that differences in shear dispersion effects across suction flowrate Q are relatively minor, especially considering only the hypothetical ultra-low Q modeled here reaches the fully-developed laminar profile before the needle terminates in the ionization chamber. However, these differences might be masked by stronger distortion effect arising from differential spatial development of the interior needle flow (Table 3 and Fig. 8) across Q, which is not accounted for in Taylor's analysis. The corresponding variability would show up in the relative suction rate U_s/U_a dependence here.

A full disentanglement of the physical mechanisms driving distortion levels, including their relative contributions and how they vary across the distortion scaling parameter S_D, is beyond the scope of the current work. Nonetheless, examining the functional form of each nondimensional parameter's contribution to S_D provides some important insights and take-away messages. These functional forms are discussed in the following three paragraphs, along with peripheral, but related and useful, discussion points.

First, the linear growth of distortion with (inverse) relative filament size ϕ/L_f shows distortion is largest for small filaments, and in fact distortion levels may often be negligible for filaments bigger than approximately 1 cm. In air, the minimum Batchelor scale L_B—describing the size of the smallest scalar structures that can exist before diffusion smears them out—is about 1 mm. Thus, while distortion levels are appreciable over only a single order of magnitude of scalar filament widths likely to occur in real plumes (depending on turbulence intensity, source geometry, and distance to source), the smallest lengthscale filaments are associated with the highest-frequency concentration fluctuations registered by a sensor. These high-frequency fluctuations are of increasing interest in many PID-related studies in olfactory neuroscience [61], in particular understanding how they are neurally encoded in the brain and translated to sensorimotor circuits to conduct behavior. Olfactometers are key components in many of these studies and are designed to deliver odor pulse trains with prescribed statistical characteristics [10, 12]. Accurate PID-based characterization of said pulse trains is critical for accurately quantifying odor stimuli.

Second, the logarithmic growth of distortion with ambient Reynolds number Re_{Ua} predicts the most sensitivity at low Re_{Ua} and a saturating response at high Re_{Ua}. We can understand this distortion mechanism by considering that even a scalar filament advecting past a non-sampling PID needle ($Q = 0$) would not result in a distortion-free interaction, due simply to the presence of the solid body of the needle in the flow. However, distortion levels become increasingly independent of ambient Reynolds number effects with increasing Re_{Ua}, similar to, for example, the friction factor in pipe flow.

Finally, the nonlinear and non-monotonic variation in distortion as a function of relative suction rate U_s/U_a is captured in the two terms of its functional contribution to S_D. These terms describe decay and slow linear growth of distortion with increasing relative suction, $2/(U_s/U_a)^{1/2}$ and $1/225(U_s/U_a)$, respectively. The decay term can be seen from Eqn. 3 to represent the relative size of the suction distortion zone ϕ/L_s. The linear growth term is throttled by the coefficient 1/225, which interestingly is equal here to the geometric ratio of the needle wall thickness δ to its length L_n (Table 1). This ratio is fixed in our models and thus we cannot explicitly test whether the linear growth coefficient is in fact more universally this geometric ratio for other PID or suction-based samplers. However, one would expect geometric ratios to show up in a robust, closed-form distortion scaling parameter based on the dimen-

sional analysis of the problem (Table 2). If true, the two terms may well represent distorting effects arising in the exterior of the flow that decay with increasing ϕ/L_s versus those arising in the orifice, entry flow, and interior needle flow regions whose effects are captured in the geometric ratio coefficient that potentially prescribes the linear growth rate in distortion in this regime. Whether or not this is true (could be tested with further modeling), the existence of a global minimum in distortion based on the non-monotonic two-term function here is an appealing draw for PID users looking for an implementable distortion mitigation strategy.

The evidence for an ideal relative suction rate that would minimize distortion across L_f and U_a was shown in the upper left panels of Figs. 11 and 12. The data points are colored by U_s/U_a and visually indicate that a value around 30 minimizes distortion levels within all L_f groups. Interestingly, two separate approaches produce seeming confirmation of a value near 30 being the universal distortion-minimizing U_s/U_a for the Aurora Scientific 200B miniPID. First, one can take the derivative of the two-term function representing distortion scaling in U_s/U_a, set it equal to zero, and solve for an ideal U_s/U_a value of 35. This is somewhat self-evident since it confirms that the two-term functional form derived here accurately captures distortion variability in relative suction rate. Alternatively, one can note the other evidence in Figs. 11 and 12 for a distortion-minimizing U_s/U_a in the vertical dashed black lines in the bottom row that indicate the distortion regime breakpoint where the filament-interface residence time in the suction distortion zone of the exterior flow equals the needle residence time of the interior flow (timescale ratio equals 1). Setting this timescale ratio equal to one and plugging in the analytical forms of each timescale (Eqns. 4 and 7), one can solve for the U_s/U_a value at the distortion breakpoint, i.e. the distortion-minimizing relative suction rate. This value is 28.

Given our intentionally idealized model design, one of the most important considerations moving forward is: how generalizeable are the findings here to suction-based sampling schemes in turbulent plumes? That is, what other parameters arise upon which distortion levels might depend when sampling non-isoaxially in a turbulent flow environment, relative to the isoaxial (both ambient flow and concentration gradient vectors parallel to the suction velocity vector/needle axis), uniform flow sampling considered herein? In the present discussion we ignore turbulent (enhanced) diffusion of scalars from the source to the exterior farfield in the vicinity of a sampling PID, and focus instead on filament-suction interaction from the exterior farfield to the sensor. Note that the effects of turbulent diffusion will produce a spectrum of scalar filaments having some characteristic distribution of sizes L_f (e.g. [62]) arriving in succession to a sampling PID, all of which interact with the sampler on a discrete filament basis. For a turbulent flow environment, the instantaneous fluid velocity at any point in space $\mathbf{u}(t)$ is composed of a mean and instantaneous (*turbulent*) velocity contribution, $\overline{\mathbf{u}}$ and $\mathbf{u}^{'}(t)$ respectively. The effects of the mean velocity can be considered analogous to the ambient flow effects here, and thus parameterize distortion through the ambient Reynolds number Re_{Ua}. The dynamic and complex, three-dimensional turbulent flow structures associated with the instantaneous velocity have the effect of not only producing a spectrum of filament widths, but also of perturbing i. the spatiotemporal structure of the suction distortion zone produced by the PID and ii. the orientation of the instantaneous scalar concentration gradient relative to the needle axis (suction velocity vector). Regardless of how exactly these effects modify distortion levels, which is no doubt complex, turbulent effects would be parameterized by a new characteristic velocity scale ratio $u_{rms}/\overline{\mathbf{u}}$, the turbulence intensity. Overall, its important to note that even in the most complex turbulent sampling environment filaments arrive at, and interact with, a sampling PID as individuals, making our findings here fundamental to understanding distortion mechanisms arising during suction-based sampling of passive scalars. In this regard, many of the findings and discussions here are broadly generalizeable to other PID and suction-based scalar samplers, and give rise to testable questions regarding the distorting role of a sampler's geometry.

5. Conclusions

We numerically modeled the geometry and sampling dynamics of a widely-used PID (Aurora Scientific 200B miniPID) to investigate how measured scalar concentration records at the sensor level compare to those registered by an ideal (non-intrusive) probe in the absence of distorting effects. We modeled idealized filament-suction interaction during PID sampling by considering a Gaussian filament advected in a steady, uniform ambient flow towards an actively sampling needle. Model runs were selected to cover a broad nondimensional parameter space containing a range of realistic sampling and plume conditions, including distorting and non-distorting regimes, relevant to a large community of PID users. We showed that PID sampling can significantly modify the peak concentration and pulse shape of sensed versus undistorted concentration records, with peak amplitude reduced by up to 45% and pulse width increased by up to 100% in the sensed records. We quantified how distortion levels vary in three key nondimensional parameters (relative suction rate, relative filament size, and ambient flow Reynolds number). We combined analytical and numerical tools, in addition to dimensional analysis and scaling arguments, to analyze, interpret, and discuss when distortion is likely and what drives it. Finally, we built robust empirical regressions capable of predicting distortion levels as a function of PID operational parameters. Our results can be used by PID users to i. estimate distortion levels based on user-specific operational conditions and ii. employ mitigation strategies, for example by adjusting the PID suction flowrate to achieve an ideal relative suction rate U_s/U_a of approximately 30. This value is shown to minimize distortion across all filament sizes and ambient flowspeeds, providing a viable mitigation strategy for the Aurora Scientific miniPID. The mechanistic insights gained into filament-suction interaction and the parameterization of associated signal distortion presented here provide insights broadly generalizeable to other suction-based PIDs and scalar samplers.

The findings of this study raise a number of important questions and ideals that will motivate future work. In the near term, we want to explore additional distortion metrics that may be of interest to the research community (e.g. the delta of the peak arrival time at the sensor relative to the ideal probe) and alternative forms of the distortion scaling parameter S_D as necessary. Going forward, we would also like to develop open-source software packages implementing our distortion models that are ultimately capable of dewarping suction-distorted PID time series data by solving the inverse problem of reconstructing the undistorted signal using the "transfer functions" derived herein. Components of this package might include functions related to signal preprocessing, filament identification and Gaussian pulse fitting, and distortion prediction. Another important line of investigation is understanding and quantifying the additional role of turbulence in suction distortion mechanisms documented here. Is there a dependence on sampler orientation angle relative to the mean ambient flow vector and/or filament concentration gradients? What is the role of turbulent fluctuations in distorting the spatial orientation of the suction distortion zone? How might we capture or understand these effects when seen through the lens of the *frozen turbulence hypothesis*? A robust means of addressing these and other questions raised herein would be to do so experimentally; laser-induced fluorescence measurements quantifying the spatiotemporal structure of undistorted filaments approaching a sampling PID simultaneously recording the sensed time series in a variety of plume/flow conditions. There are also a number of interesting questions concerning application of our distortion model to suction-based passive scalar samplers operating in aqueous environments, stemming in large part from the dimensional analysis and dimensionless suction distortion model provided herein (Table 2, Eqn. 18). For example, what is the role of Schmidt number Sc (Eqn. 12) which increases by approximately three orders of magnitude in aqueous versus gaseous environments due to the much-reduced scalar diffusivities there? Higher Sc translates to smaller filaments, and thus likely higher levels of distortion. However, increased fluid density and viscosity in aqueous environments may necessitate larger intake (e.g. needle) diameters and/or reduced suction velocities as constrained by pumping energetics. In summary, testing the application of our distortion model to an extended range of the distortion scaling parameter S_D and/or including the effects of other potentially-relevant nondimensional parameters would aid in testing how generalizeable of our distortion model is to understanding passive scalar distortion during suction-based sampling schemes across working fluids and scalar entities, sampler geometries and suction rates, and diverse environmental plume conditions.

Acknowledgements

This project is supported by the NSF/CIHR/DFG/FRQ/UKRI-MRC Next Generation Networks for Neuroscience Program (Award Number 2014217). Additional support comes from the NIH and NSF Odor Plume Neurophotonics (OPeN) Teams (Award Numbers: NIH BRAIN 1UF1NS116241-01 and NSF BCS 1926668). We would like to thank our many collaborators on these team science efforts for numerous stimulating conversations and thoughtful feedback. We would also like to thank Dio Beck and other members of the Crimaldi Group for many fruitful interactions over the course of this work.

References

[1] J. A. Riffell, L. Abrell, J. G. Hildebrand, Physical processes and real-time chemical measurement of the insect olfactory environment, Journal of chemical ecology 34 (7) (2008) 837–853.

[2] S. B. Olsson, L. S. Kuebler, D. Veit, K. Steck, A. Schmidt, M. Knaden, B. S. Hansson, A novel multicomponent stimulus device for use in olfactory experiments, Journal of Neuroscience Methods 195 (1) (2011) 1–9.

[3] E. Yee, P. Kosteniuk, G. Chandler, C. Biltoft, J. Bowers, Statistical characteristics of concentration fluctuations in dispersing plumes in the atmospheric surface layer, Boundary-Layer Meteorology 65 (1) (1993) 69–109.

[4] K. A. Justus, J. Murlis, C. Jones, R. T. Cardé, Measurement of odor-plume structure in a wind tunnel using a photoionization detector and a tracer gas, Environmental Fluid Mechanics 2 (1) (2002) 115–142.

[5] E. G. Connor, M. K. McHugh, J. P. Crimaldi, Quantification of airborne odor plumes using planar laser-induced fluorescence, Experiments in Fluids 59 (9) (2018) 1–11.

[6] K. A. Justus, R. T. Cardé, A. S. French, Dynamic properties of antennal responses to pheromone in two moth species, Journal of neurophysiology 93 (4) (2005) 2233–2239.

[7] K. I. Nagel, R. I. Wilson, Biophysical mechanisms underlying olfactory receptor neuron dynamics, Nature neuroscience 14 (2) (2011) 208–216.

[8] D. H. Gire, V. Kapoor, A. Arrighi-Allisan, A. Seminara, V. N. Murthy, Mice develop efficient strategies for foraging and navigation using complex natural stimuli, Current Biology 26 (10) (2016) 1261–1273.

[9] E. Álvarez-Salvado, A. M. Licata, E. G. Connor, M. K. McHugh, B. M. King, N. Stavropoulos, J. D. Victor, J. P. Crimaldi, K. I. Nagel, Elementary sensory-motor transformations underlying olfactory navigation in walking fruit-flies, Elife 7 (2018) e37815.

[10] S. Gorur-Shandilya, C. Martelli, M. Demir, T. Emonet, Controlling and measuring dynamic odorant stimuli in the laboratory, Journal of Experimental Biology 222 (23) (2019).

[11] A. Gumaste, G. Coronas-Samano, J. Hengenius, R. Axman, E. Connor, K. Baker, B. Ermentrout, J. Crimaldi, J. Verhagen, A comparison between mouse, in silico, and robot odor plume navigation reveals advantages of mouse odor tracking, Eneuro 7 (1) (2020).

[12] T. Ackels, A. Erskine, D. Dasgupta, A. C. Marin, T. P. Warner, S. Tootoonian, I. Fukunaga, J. J. Harris, A. T. Schaefer, Fast odour dynamics are encoded in the olfactory system and guide behaviour, Nature 593 (7860) (2021) 558–563.

[13] K. A. Justus, S. W. Schofield, J. Murlis, R. T. Carde, Flight behaviour of cadra cautella males in rapidly pulsed pheromone plumes, Physiological Entomology 27 (1) (2002) 58–66.

[14] K. R. Mylne, P. Mason, Concentration fluctuation measurements in a dispersing plume at a range of up to 1000 m, Quarterly Journal of the Royal Meteorological Society 117 (497) (1991) 177–206.

[15] F. Drewnick, T. Böttger, S.-L. Weiden-Reinmüller, S. Zorn, T. Klimach, J. Schneider, S. Borrmann, Design of a mobile aerosol research laboratory and data processing tools for effective stationary and mobile field measurements, Atmospheric Measurement Techniques 5 (6) (2012) 1443–1457.

[16] J. Burgués, S. Marco, Environmental chemical sensing using small drones: A review, Science of The Total Environment (2020) 141172.

[17] P. Hobbs, T. Misselbrook, B. Pain, Assessment of odours from livestock wastes by a photoionization detector, an electronic nose, olfactometry and gas chromatography-mass spectrometry, Journal of Agricultural Engineering Research 60 (2) (1995) 137–144.

[18] E. Yee, C. A. Biltoft, Concentration fluctuation measurements in a plume dispersing through a regular array of obstacles, Boundary-Layer Meteorology 111 (3) (2004) 363–415.

[19] J. Lovelock, A photoionization detector for gases and vapours, Nature 188 (4748) (1960) 401–401.
[20] F. Peng, P. Xie, Y. Shi, J. Wang, W. Liu, H. Li, Photoionization detector for portable rapid gc, Chromatographia 65 (5) (2007) 331–336.
[21] S. O. Agbroko, J. Covington, A novel, low-cost, portable pid sensor for the detection of volatile organic compounds, Sensors and Actuators B: Chemical 275 (2018) 10–15.
[22] G. C. Rezende, S. Le Calvé, J. J. Brandner, D. Newport, Micro photoionization detectors, Sensors and Actuators B: Chemical 287 (2019) 86–94.
[23] J. N. Driscoll, Evaluation of a new photoionization detector for organic compounds, Journal of Chromatography A 134 (1) (1977) 49–55.
[24] J. Driscoll, Review of photoionization detection in gas chromatography: the first decade, Journal of chromatographic science 23 (11) (1985) 488–492.
[25] A. C. True, J. P. Crimaldi, Hydrodynamics of viscous inhalant flows, Physical Review E 95 (5) (2017) 053107.
[26] E. Connor, A. True, J. Crimaldi, Dynamics of an idealized respiratory-type flow: Tidal exchange across intermediate reynolds numbers, Physical Review Fluids 5 (9) (2020) 093103.
[27] Z. Pan, J. K. Nunes, H. A. Stone, Regime map and triple point in selective withdrawal, Physical Review Letters 125 (26) (2020) 264502.
[28] T. L. Spencer, A. Clark, J. Fonollosa, E. Virot, D. L. Hu, Sniffing speeds up chemical detection by controlling air-flows near sensors, Nature communications 12 (1) (2021) 1–10.
[29] S. Belyaev, L. Levin, Techniques for collection of representative aerosol samples, Journal of Aerosol Science 5 (4) (1974) 325–338.
[30] S. Belyaev, L. Levin, Investigation of aerosol aspiration by photographing particle tracks under flash illumination, Journal of Aerosol Science 3 (2) (1972) 127–140.
[31] S. K. Zaripov, L. Zigangareeva, O. Kiselev, Aerosol aspiration into a tube from a calm medium, Fluid dynamics 35 (2) (2000) 242–246.
[32] S. Dunnett, X. Wen, A numerical study of the sampling efficiency of a tube sampler operating in calm air facing both vertically upwards and downwards, Journal of aerosol science 33 (12) (2002) 1653–1665.
[33] S. Grinshpun, K. Willeke, S. Kalatoor, A general equation for aerosol aspiration by thin-walled sampling probes in calm and moving air, Atmospheric Environment. Part A. General Topics 27 (9) (1993) 1459–1470.
[34] J. L. Jimenez, J. T. Jayne, Q. Shi, C. E. Kolb, D. R. Worsnop, I. Yourshaw, J. H. Seinfeld, R. C. Flagan, X. Zhang, K. A. Smith, et al., Ambient aerosol sampling using the aerodyne aerosol mass spectrometer, Journal of Geophysical Research: Atmospheres 108 (D7) (2003).
[35] L. Williams, L. Gonzalez, J. Peck, D. Trimborn, J. McInnis, M. Farrar, K. Moore, J. Jayne, W. Robinson, D. Lewis, et al., Characterization of an aerodynamic lens for transmitting particles greater than 1 micrometer in diameter into the aerodyne aerosol mass spectrometer, Atmospheric Measurement Techniques 6 (11) (2013) 3271–3280.
[36] S. Von der Weiden, F. Drewnick, S. Borrmann, et al., Particle loss calculator–a new software tool for the assessment of the performance of aerosol inlet systems, Atmos. Meas. Tech 2 (2) (2009) 479–494.
[37] M. Aubinet, T. Vesala, D. Papale, Eddy covariance: a practical guide to measurement and data analysis, Springer Science & Business Media, 2012.
[38] J. Wyngaard, The effects of probe-induced flow distortion on atmospheric turbulence measurements: Extension to scalars, Journal of Atmospheric Sciences 45 (22) (1988) 3400–3412.
[39] J. Wyngaard, Flow-distortion effects on scalar flux measurements in the surface layer: implications for sensor design, Boundary-layer meteorology 42 (1) (1988) 19–26.
[40] M. Metzger, J. Klewicki, Development and characterization of a probe to measure scalar transport, Measurement Science and Technology 14 (8) (2003) 1437.
[41] S. Dunnett, D. Ingham, A mathematical theory to two-dimensional blunt body sampling, Journal of aerosol science 17 (5) (1986) 839–853.
[42] G. I. Taylor, Dispersion of soluble matter in solvent flowing slowly through a tube, Proceedings of the Royal Society of London. Series A. Mathematical and Physical Sciences 219 (1137) (1953) 186–203.
[43] D. Lenschow, M. Raupach, The attenuation of fluctuations in scalar concentrations through sampling tubes, Journal of Geophysical Research: Atmospheres 96 (D8) (1991) 15259–15268.
[44] R. L. Panton, Incompressible flow, John Wiley & Sons, 2013.
[45] R. K. Brayton, F. G. Gustavson, G. D. Hachtel, A new efficient algorithm for solving differential-algebraic systems using implicit backward differentiation formulas, Proceedings of the IEEE 60 (1) (1972) 98–108.
[46] A. C. Hindmarsh, P. N. Brown, K. E. Grant, S. L. Lee, R. Serban, D. E. Shumaker, C. S. Woodward, Sundials: Suite of nonlinear and differential/algebraic equation solvers, ACM Transactions on Mathematical Software (TOMS) 31 (3) (2005) 363–396.
[47] P. Deuflhard, A modified newton method for the solution of ill-conditioned systems of nonlinear equations with application to multiple shooting, Numerische Mathematik 22 (4) (1974) 289–315.
[48] Y. Saad, M. H. Schultz, Gmres: A generalized minimal residual algorithm for solving nonsymmetric linear systems, SIAM Journal on scientific and statistical computing 7 (3) (1986) 856–869.
[49] A. Greenbaum, Iterative methods for solving linear systems, SIAM, 1997.
[50] Y. Saad, Iterative methods for sparse linear systems, SIAM, 2003.
[51] M. L. Parks, E. De Sturler, G. Mackey, D. D. Johnson, S. Maiti, Recycling krylov subspaces for sequences of linear systems, SIAM Journal on Scientific Computing 28 (5) (2006) 1651–1674.
[52] W. Hackbusch, Multi-grid methods and applications, Vol. 4, Springer Science & Business Media, 2013.
[53] M. Raffel, C. E. Willert, F. Scarano, C. J. Kähler, S. T. Wereley, J. Kompenhans, Particle image velocimetry: a practical guide, Springer, 2018.
[54] A. C. True, J. P. Crimaldi, High dynamic range particle image velocimetry analysis of viscous inhalant flows, Physics of Fluids 31 (10) (2019) 103605.
[55] A. Reci, A. J. Sederman, L. F. Gladden, Experimental evidence of velocity profile inversion in developing laminar flow using magnetic resonance velocimetry, Journal of Fluid Mechanics 851 (2018) 545–557.
[56] H. D. Haustein, B. Kashi, Distortion of pipe-flow development by boundary layer growth and unconstrained inlet conditions, Physics of Fluids 31 (6) (2019) 063602.
[57] S. P. Sutera, R. Skalak, The history of poiseuille's law, Annual Review of Fluid Mechanics 25 (1) (1993) 1–20.
[58] A. Mohanty, S. Asthana, Laminar flow in the entrance region of a smooth pipe, Journal of Fluid Mechanics 90 (3) (1979) 433–447.
[59] N. Dombrowski, E. Foumeny, S. Ookawara, A. Riza, The influence of reynolds number on the entry length and pressure drop for laminar pipe flow, The Canadian Journal of Chemical Engineering 71 (3) (1993) 472–476.
[60] F. Durst, S. Ray, B. Ünsal, O. Bayoumi, The development lengths of laminar pipe and channel flows, Journal of Fluids Engineering 127 (6) (2005) 1154–1160.
[61] J. Crimaldi, H. Lei, A. Schaefer, M. Schmuker, B. H. Smith, A. C. True, J. V. Verhagen, J. D. Victor, Active sensing in a dynamic olfactory world, Journal of computational neuroscience 50 (1) (2022) 1–6.
[62] A. Celani, E. Villermaux, M. Vergassola, Odor landscapes in turbulent environments, Physical Review X 4 (4) (2014) 041015.

Appendix A. Model runs

Table A.6: Distortion model cases run, summarizing the relevant parameter space covered including filament size L_f, ambient flowspeed U_a, PID suction rate Q, relative suction rate, U_s/U_a, and the suction and ambient Reynolds (Re_{U_s} and Re_{U_a}, respectively) and Péclet (Pe_{U_s} and Pe_{U_a}, respectively) numbers. The parameter space covered is relevant to many problems in olfaction and odor plume dynamics and extensively explores both distorting and non-distorting PID operational regimes.

case	L_f [mm]	U_a [m/s]	Q [L/min]	U_s [m/s]	U_s/U_a	Re_{U_s}	Re_{U_a}	Pe_{U_s}	Pe_{U_a}
1	2	0.225	0.5	18.370	81.643	945	12	1126	14
2	2	0.235	0.225	8.266	35.176	425	12	507	14
3	2	0.350	0.225	8.266	23.618	425	18	507	21
4	2	0.350	0.9	33.065	94.473	1701	18	2027	21
5	2	0.400	0.5	18.370	45.924	945	21	1126	25
6	2	0.500	0.225	8.266	16.533	425	26	507	31
7	2	0.500	0.9	33.065	66.131	1701	26	2027	31
8	2	0.500	1.2	44.087	88.174	2268	26	2702	31
9	2	0.500	1.5	55.109	110.218	2835	26	3378	31
10	2	0.550	0.225	8.266	15.030	425	28	507	34
11	2	0.600	0.225	8.266	13.777	425	31	507	37
12	2	0.690	0.225	8.266	11.980	425	35	507	42
13	2	0.750	0.225	8.266	11.022	425	39	507	46
14	2	0.800	0.5	18.370	22.962	945	41	1126	49
15	2	0.827	0.225	8.266	10.000	425	43	507	51
16	2	0.900	1.2	44.087	48.986	2268	46	2702	55
17	2	1.000	0.225	8.266	8.266	425	51	507	61
18	2	1.000	0.9	33.065	33.065	1701	51	2027	61
19	2	1.000	1.5	55.109	55.109	2835	51	3378	61
20	2	1.200	0.4	14.696	12.246	756	62	901	74
21	2	1.400	0.5	18.370	13.121	945	72	1126	86
22	2	1.400	1.5	55.109	39.364	2835	72	3378	86
23	2	1.800	0.9	33.065	18.370	1701	93	2027	110
24	2	1.800	1.5	55.109	30.616	2835	93	3378	110
25	2	2.200	1.2	44.087	20.040	2268	113	2702	135
26	2	2.500	0.9	33.065	13.226	1701	129	2027	153
27	2	2.500	1.5	55.109	22.044	2835	129	3378	153
28	2	3.000	1.2	44.087	14.696	2268	154	2702	184
29	2	3.500	1.5	55.109	15.745	2835	180	3378	215
30	5	0.200	0.225	8.266	41.332	425	10	507	12
31	5	0.225	0.5	18.370	81.643	945	12	1126	14
32	5	0.300	0.9	33.065	110.218	1701	15	2027	18
33	5	0.850	1.5	55.109	64.834	2835	44	3378	52
34	5	1.000	0.225	8.266	8.266	425	51	507	61
35	5	1.000	0.5	18.370	18.370	945	51	1126	61
36	5	1.500	1.2	44.087	29.391	2268	77	2702	92
37	5	5.000	1.5	55.109	11.022	2835	257	3378	306
38	10	0.500	1.5	55.109	110.218	2835	26	3378	31
39	10	0.500	0.225	8.266	16.533	425	26	507	31
40	10	0.500	0.9	33.065	66.131	1701	26	2027	31
41	10	0.500	1.2	44.087	88.174	2268	26	2702	31
42	10	0.827	0.225	8.266	10.000	425	43	507	51
43	10	1.000	0.225	8.266	8.266	425	51	507	61
44	10	1.000	0.9	33.065	33.065	1701	51	2027	61
45	10	1.000	1.5	55.109	55.109	2835	51	3378	61
46	10	1.400	0.5	18.370	13.121	945	72	1126	86

Aaron True: Aaron completed his PhD in Civil and Environmental Engineering (Environmental Fluid Mechanics) at the Georgia Institute of Technology in 2014. He joined Professor John Crimaldi's group at the University of Colorado that year. He currently conducts studies of fluid flow and odor transport using particle image velocimetry (PIV), laser-induced fluorescence (LIF), and computational fluid dynamics (CFD) on the NSF NeuroNex Odor2Action Network.

John Crimaldi: John completed his PhD in Civil and Environmental Engineering (Environmental Fluid Mechanics) at Stanford University in 1998. He joined the faculty of Civil, Environmental, and Architectural Engineering at the University of Colorado Boudler shortly thereafter, and built a research group focused on turbulence, mixing and transport phenomena, and experimental fluid mechanics. Currently he is a Professor and Associate Chair for Graduate Education of the same department, and serves as the Principal Investigator for the NSF NeuroNex Odor2Action Network.

CRediT authorship contribution statement

Aaron True: Conceptualization, Methodology, Investigation, Validation, Software, Formal analysis, Visualization, Writing – original draft, Writing – review & editing.

John Crimaldi: Conceptualization, Methodology, Resources, Writing – review & editing, Supervision, Project administration, Funding acquisition

Declaration of interests

☒The authors declare that they have no known competing financial interests or personal relationships that could have appeared to influence the work reported in this paper.

☐The authors declare the following financial interests/personal relationships which may be considered as potential competing interests: